# **OPEN ACCESS**



# Morphologies of Galaxies at $z \gtrsim 9$ Uncovered by JWST/NIRCam Imaging: Cosmic Size Evolution and an Identification of an Extremely Compact Bright Galaxy at $z \sim 12$

Yoshiaki Ono 1 , Yuichi Harikane 1 , Masami Ouchi 1,2,3 , Hidenobu Yajima 4 , Makito Abe 4, Yuki Isobe 1,5 , Takatoshi Shibuya 6, John H. Wise 7 , Yechi Zhang 1,8 , Kimihiko Nakajima 2 , and Hiroya Umeda 1,5 , Institute for Cosmic Ray Research, The University of Tokyo, 5-1-5 Kashiwanoha, Kashiwa, Chiba 277-8582, Japan 2 National Astronomical Observatory of Japan, 2-21-1 Osawa, Mitaka, Tokyo 181-8588, Japan 3 Kavli Institute for the Physics and Mathematics of the Universe (WPI), The University of Tokyo, 5-1-5 Kashiwanoha, Kashiwa-shi, Chiba, 277-8583, Japan 4 Center for Computational Sciences, University of Tsukuba, Ten-nodai, 1-1-1 Tsukuba, Ibaraki 305-8577, Japan 5 Department of Physics, Graduate School of Science, The University of Tokyo, 7-3-1 Hongo, Bunkyo, Tokyo 113-0033, Japan 6 Kitami Institute of Technology, 165 Koen-cho, Kitami, Hokkaido 090-8507, Japan 7 Center for Relativistic Astrophysics, School of Physics, Georgia Institute of Technology, Atlanta, GA 30332, USA 8 Department of Astronomy, Graduate School of Science, the University of Tokyo, 7-3-1 Hongo, Bunkyo, Tokyo 113-0033, Japan Received 2022 August 29; revised 2023 April 13; accepted 2023 May 9; published 2023 July 4

### **Abstract**

We present morphologies of galaxies at  $z\gtrsim 9$  resolved by JWST/NIRCam 2–5  $\mu$ m imaging. Our sample consists of 22 galaxy candidates identified by stringent dropout and photo-z criteria in GLASS, CEERS, SMACS J0723, and Stephan's Quintet flanking fields, one of which has been spectroscopically identified at z=11.44. We perform surface brightness (SB) profile fitting with GALFIT for six bright galaxies with a signal-to-noise ratio = 10–40 on an individual basis and for stacked faint galaxies with secure point-spread functions (PSFs) of the NIRCam real data, carefully evaluating systematics by Monte Carlo simulations. We compare our results with those of previous JWST studies, and confirm that the effective radii  $r_{\rm e}$  of our measurements are consistent with those of previous measurements at  $z\sim 9$ . We obtain  $r_{\rm e}\simeq 200$ –300 pc with the exponential-like profiles, Sérsic indexes of  $n\simeq 1$ –1.5, for galaxies at  $z\sim 12$ –16, indicating that the relation of  $r_{\rm e}\propto (1+z)^s$  for  $s=-1.22^{+0.17}_{-0.16}$  explains cosmic evolution over  $z\sim 0$ –16 for  $\sim L_{z=3}^*$  galaxies. One bright ( $M_{\rm UV}=-21$  mag) galaxy at  $z\sim 12$ , GL-z12-1, has an extremely compact profile with  $r_{\rm e}=39\pm 11$  pc that is surely extended over the PSF. Even in the case that the GL-z12-1 SB is fit by active galactic nuclei + galaxy composite profiles, the best-fit galaxy component is again compact,  $r_{\rm e}=48^{+38}_{-15}$  pc, which is significantly (>5 $\sigma$ ) smaller than the typical  $r_{\rm e}$  value at  $z\sim 12$ . Compared with numerical simulations, we find that such a compact galaxy naturally forms at  $z\gtrsim 10$ , and that frequent mergers at the early epoch produce more extended galaxies following the  $r_{\rm e}\propto (1+z)^s$  relation.

*Unified Astronomy Thesaurus concepts:* Galactic and extragalactic astronomy (563); Galaxies (573); Galaxy radii (617); Galaxy structure (622); Galaxy formation (595); Galaxy evolution (594); Lyman-break galaxies (979); High-redshift galaxies (734)

## 1. Introduction

JWST (Gardner et al. 2023) has opened the redshift frontier by providing deep infrared images with unprecedented high sensitivity and resolution (e.g., Pontoppidan et al. 2022). Early studies have reported dozens of high-z galaxies candidates at  $z \sim 9-16$  (Castellano et al. 2022; Naidu et al. 2022a; Adams et al. 2023; Atek et al. 2023; Leethochawalit et al. 2023; Yan et al. 2023) and the evolution of the UV luminosity density and the stellar mass density at very early epochs (Finkelstein et al. 2022; Labbe et al. 2023; Donnan et al. 2023; Harikane et al. 2023; see also, Inayoshi et al. 2022; Lovell et al. 2023) as well as their various galaxy properties such as star formation histories and UV continuum slopes have begun to be discussed (Topping et al. 2022; Cullen et al. 2023; Furtak et al. 2023; Whitler et al. 2023; see also, Nanayakkara et al. 2023).

Characterizing the evolution of galaxy sizes is useful for understanding galaxy formation history (Conselice 2014). Before the arrival of JWST, the sizes of galaxies at  $z \sim 7-10$  have been measured based on deep near-infrared images taken with the

Original content from this work may be used under the terms of the Creative Commons Attribution 4.0 licence. Any further distribution of this work must maintain attribution to the author(s) and the title of the work, journal citation and DOI.

Hubble Space Telescope (HST) and their size–luminosity relation and the size evolution have been intensively investigated (e.g., Oesch et al. 2010; Grazian et al. 2012; Ono et al. 2013; Kawamata et al. 2015, 2018; Holwerda et al. 2015, 2020; Shibuya et al. 2015; Curtis-Lake et al. 2016; Allen et al. 2017; Bowler et al. 2017; Bouwens et al. 2017, 2021, 2022; Salmon et al. 2018; Bridge et al. 2019). Based on the size measurement results with HST legacy data for about 190,000 galaxies at  $z \sim 0$ –10, Shibuya et al. (2015) performed a power-law fitting for the size-luminosity relation, and found that the slope of the power law is almost constant,  $\alpha = -0.27 \pm 0.01$ , and the characteristic half-light radius at  $M_{\rm UV} = -21.0$  mag becomes smaller with increasing redshift scaling as  $\propto (1+z)^{-1.20\pm0.04}$ . Now that JWST has allowed us to find galaxies with similar luminosities at even higher redshifts thanks to the better sensitivity and longer wavelength coverage, and to obtain more accurate size measurements because of the better spatial resolution compared to HST, it would be interesting to investigate if this trend continues toward higher redshifts, to study star formation activities in galaxies well before the end of the cosmic reionization (Ouchi et al. 2020; Planck Collaboration et al. 2020; Robertson 2022). Recently, theoretical studies tailored for JWST observations for galaxies at lower redshifts z = 3-6 based on cosmological simulations have been reported (Costantin et al. 2023), and comparisons with such theoretical study results are

expected to become increasingly important as JWST data are obtained.

In this paper, we investigate sizes of galaxies at  $z \sim 9-16$  with deep JWST NIRCam (Rieke et al. 2005) images based on the high-z galaxy candidate samples constructed by Harikane et al. (2023), who selected F115W, F150W, and F200W dropouts from the JWST deep imaging data publicly available so far taken by four Early Release Science (ERS) and Early Release Observation (ERO; Pontoppidan et al. 2022) programs: ERS Grism Lens-Amplified Survey from Space (GLASS; Treu et al. 2022), ERS The Cosmic Evolution Early Release Science (CEERS; Finkelstein et al. 2022), ERO SMACS J0723, and ERO Stephan's Quintet.

This paper is outlined as follows. In Section 2, we introduce the high-z galaxy samples and summarize the NIRCam imaging data used in this study. In Section 3, the surface brightness (SB) profile fitting is described and Monte Carlo (MC) simulations are conducted to take into account the systematic and statistical uncertainties in the profile fitting. We present size and total magnitude measurement results in the rest-frame UV and optical with object-by-object comparisons with previous results, and then investigate the size-luminosity relation and the size evolution in Section 4. We discuss the physical origin of very compact galaxy candidates and compare our results with cosmological simulation results in Section 5. We summarize our work in Section 6. Throughout this paper, we use magnitudes in the AB system (Oke & Gunn 1983) and assume a flat universe with  $\Omega_{\rm m} = 0.3$ ,  $\Omega_{\Lambda} = 0.7$ , and  $H_0 = 70$  km s<sup>-1</sup> Mpc<sup>-1</sup>. In this cosmological model, an angular dimension of 1."0 corresponds to a physical dimension of 4.463 kpc at z = 9.0, 3.659 kpc at z = 12.0, and  $2.953 \,\mathrm{kpc}$  at z = 16.0 (e.g., Equation (18) of Hogg 1999). Following the previous work, we express galaxy UV luminosities in units of the characteristic luminosity of  $z \sim 3$  galaxies,  $L_{z=3}^*$ , which corresponds to  $M_{\rm UV} = -21.0$  mag (Steidel et al. 1999).

# 2. Data and Samples

We measure sizes of the  $z\sim9$ –16 galaxy candidates selected in Harikane et al. (2023) from four JWST NIRCam early deep public data sets by the ERS and ERO programs: ERS GLASS, ERS CEERS, ERO SMACS J0723, and ERO Stephan's Quintet. See Harikane et al. (2023) for details of the imaging data sets and the sample construction. Briefly,  $z\sim9$  galaxy candidates (F115W dropouts) are selected by

$$(F115W - F150W > 1.0) \land ,$$
 (1)

$$(F150W - F277W < 1.0) \land ,$$
 (2)

$$(F115W - F150W > (F150W - F277W) + 1.0),$$
 (3)

 $z \sim 12$  galaxy candidates (F150W dropouts) are selected by

$$(F150W - F200W > 1.0) \land ,$$
 (4)

$$(F200W - F356W < 1.0) \land ,$$
 (5)

$$(F150W - F200W > (F200W - F356W) + 1.0),$$
 (6)

and  $z \sim 16$  galaxy candidates (F200W dropouts) are selected by

$$(F200W - F277W > 1.0),$$
 (7)

$$(F277W - F444W < 1.0),$$
 (8)

$$(F200W - F277W > 1.5(F277W - F444W) + 1.0).$$
 (9)

These colors are measured with fixed apertures in point-spread function (PSF) matched multi-band images. Null detection criteria

in bluer bands than the Lyman break, and a SExtractor (Bertin & Arnouts 1996) stellarity parameter criterion, CLASS STAR <0.9, are also applied. In addition, based on the results with the CEERS simulated images (Somerville et al. 2021; Yung et al. 2022), it is required that the difference between  $\chi^2$  values of high-z and low-z solutions for our candidates calculated by a photometric redshift code exceed 9, i.e.,  $\Delta \chi^2 > 9$ , which is more strict than the frequently adopted criterion of  $\Delta \chi^2 > 4$ , to better exclude low-z interlopers (for details, see Section 3.3 of Harikane et al. 2023). As a result, reliable samples of high-z galaxy candidates are constructed; the numbers of F115W dropouts, F150W dropouts, and F200W dropouts are 13, 8, and 1, respectively. 10 Among these dropouts, CR2-z12-1 (Maisie's Galaxy, Finkelstein et al. 2022) has been spectroscopically identified at z = 11.44 with JWST/NIRSpec (Arrabal Haro et al. 2023), whose spectroscopic redshift is consistent with the previous photometric redshift estimates. Tables 1–3 summarize  $z \sim 9$ ,  $\sim 12$ , and  $\sim 16$  galaxy candidates used in our size analyses, respectively.

To minimize the effects of morphological K correction in comparison with the previous work, we measure galaxy sizes with NIRCam images that are closest to the rest frame  $1600-1700\,\text{Å}$ . Specifically, we use F150W images for  $z\sim9$  galaxy candidates, F200W images for  $z\sim12$  galaxy candidates, and F277W images for  $z\sim16$  galaxy candidates (Figure 1). In addition, we use F444W images to measure the rest-frame optical  $(4000-5000\,\text{Å})$  sizes for  $z\sim9$  galaxy candidates. The pixel scale of the NIRCam images is  $0.015\,\text{pix}^{-1}$ , except for the ERO Stephan's Quintet field, where the pixel scale is  $0.0030\,\text{pix}^{-1}$  to reduce the image size. Their  $5\sigma$  and  $10\sigma$  limiting magnitudes are summarized in Table 4.

We use empirical PSFs created by stacking bright point sources in the NIRCam real images. For this purpose, we select 7-15 unsaturated bright point sources with  $\simeq$ 22–24.5 mag in each field. PSFs can also be generated by using WebbPSF (Perrin et al. 2012, 2014). We created PSFs with WebbPSF by using a jitter value of 4.1 mas, which corresponds to the square root of the sum of the squares of the pointing stability (1 mas) and dithering accuracy (4 mas at most), as described in Sections 3.3 and 3.4 of Rigby et al. (2023). However, as shown in Figure 2, we find that the FWHMs of PSFs generated with WebbPSF are smaller than the smallest FWHMs of bright point objects detected in the NIRCam real images, indicating that the model PSFs are sharper than the actual PSFs. This is probably just because the PSFs created with WebbPSF here are not drizzled, although they should be drizzled in the same way as the science data (see also, Tacchella et al. 2023). We thus use the empirically created PSFs in this study. Table 4 presents the PSF FWHMs and Figure 3 shows the PSFs in F150W, F200W, and F444W for the GLASS field as examples. The variation of point-source FWHMs between different fields is not large; in F200W, the difference is at most  $\simeq 4\%$  (=[0.0795 -0.0765]/0.0765 × 100).

To obtain reliable galaxy size estimates, Mosleh et al. (2012) reported that a signal-to-noise ratio (S/N) of 10 is needed, because SB profile fittings require a significant detection in not only the central region of sources, but also the outer structures. We thus analyze our dropouts individually down to an S/N of 10 for their apparent magnitudes measured in 0.0%2 diameter

<sup>&</sup>lt;sup>9</sup> In this case,  $0.048L_{z=3}^*$ ,  $0.12L_{z=3}^*$  and  $0.3L_{z=3}^*$  correspond to  $M_{\rm UV}=-17.7$ , -18.7, and -19.7 mag, respectively.

 $<sup>\</sup>overline{^{10}}$  CR2-z16-1 (CEERS-93316, Donnan et al. 2023; see also, Naidu et al. 2022b) is excluded from our analyses because it has been spectroscopically identified as a strong line emitter at z=4.912 (Arrabal Haro et al. 2023).

ID	R.A. (hh:mm:ss)	Decl. (dd:mm:ss)	$z_{ m photo}$	$m_{ m UV}^{ m (ap)}$ (mag)	m <sub>opt</sub> <sup>(ap)</sup> (mag)	M <sub>UV</sub> (mag)
(1)	(2)	(3)	(4)	(5)	(6)	(7)
-		$L_{/}$	$L_{z=3}^* = 0.3-1$			
GL-z9-1	00:14:02.85	-30:22:18.6	$10.49^{+0.53}_{-0.72}$	27.9	27.6	-20.9
		L/L	$^*_{z=3} = 0.12 - 0.3$			
GL-z9-2	00:14:03.28	-30:21:05.6	$10.46^{+0.45}_{-0.99}$	29.6	29.6	-19.7
GL-z9-4	00:14:00.27	-30:21:25.9	$10.19_{-0.55}^{+0.63}$	29.2	29.9	-19.4
GL-z9-6	00:14:04.37	-30:20:39.6	$8.97^{+0.36}_{-0.36}$	29.6	29.7	-18.9
GL-z9-3	00:14:00.09	-30:19:06.9	$8.93^{+0.39}_{-0.38}$	29.5	29.0	-18.8
GL-z9-5	00:14:03.10	-30:22:26.3	$8.69^{+0.42}_{-0.15}$	29.4	29.7	-18.8
		$L/L_z^*$	$\frac{c}{c} = 3 = 0.048 - 0.12$			
GL-z9-11	00:14:02.49	-30:22:00.9	$9.89^{+0.21}_{-0.74}$	29.2	30.3	-18.6
GL-z9-7	00:14:02.52	-30:21:57.0	$10.32^{+0.74}_{-0.82}$	29.8	29.3	-18.2
GL-z9-10	00:14:03.47	-30:19:00.9	$8.73^{+0.68}_{-0.41}$	29.7	29.8	-18.2
GL-z9-12	00:14:06.85	-30:22:02.0	$9.07^{+1.02}_{-0.23}$	29.9	30.3	-18.2
GL-z9-8	00:14:00.83	-30:21:29.8	$9.08^{+0.94}_{-0.32}$	29.3	30.4	-18.1
GL-z9-9	00:14:03.71	-30:21:03.6	$9.27^{+1.28}_{-0.61}$	29.9	29.9	-18.1
GL-z9-13	00:13:57.45	-30:18:00.0	$8.74^{+0.57}_{-0.28}$	29.2	30.1	-18.1

Note. The values presented in this table have been obtained from Harikane et al. (2023). (1) Object ID. (2) R.A. (3) decl. (4) Photometric redshift. (5) Aperture magnitude in F150W measured in 0.12 diameter circular aperture. (6) Aperture magnitude in F444W measured in 0.12 diameter circular aperture. (7) Total absolute UV magnitude.

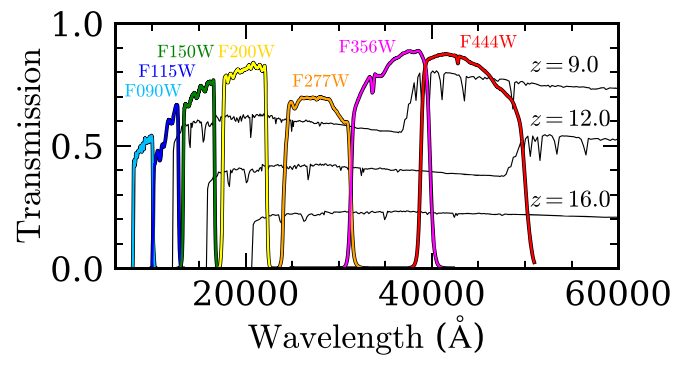


**Figure 1.** Transmissions of the seven NIRCam broadband filters (cyan: F090W, blue: F115W, green: F150W, yellow: F200W, orange: F277W, magenta: F356W, red: F444W) together with three spectra of SFGs at z = 9.0, 12.0, and 16.0 from the Bruzual & Charlot (2003) library (black lines).

circular apertures. Namely, the object IDs that show S/N > 10 are GL-z9-1 in the F115W-dropout sample, GL-z12-1, CR2-z12-1, CR2-z12-2, and CR2-z12-3 in the F150W-dropout sample, and S5-z16-1 in the F200W-dropout sample. For the rest-frame optical analyses, we individually investigate GL-z9-1, which is the only object in our F115W-dropout sample showing an aperture magnitude brighter than  $10\sigma$  in F444W.

To extend our size measurements to fainter objects, we divide the samples into three luminosity bins,  $L/L_{z=3}^* = 0.3-1$ ,  $L/L_{z=3}^* = 0.12-0.3$ , and  $L/L_{z=3}^* = 0.048-0.12$  based on their  $M_{\rm UV}$  magnitudes as listed in Tables 1 and 2, and make median-stacked images separately for the second and third brightest luminosity bins. The number of F115W dropouts (F150W dropouts) with  $L/L_{z=3}^* = 0.12-0.3$  is five (3), and the number with  $L/L_{z=3}^* = 0.048-0.12$  is seven (2). We confirm that the S/Ns of the aperture magnitudes of the stacked objects are  $\gtrsim 10$ .

The stacked F150W dropout with  $L/L_{z=3}^* = 0.048-0.12$  is not used in this study, because the number of objects in this luminosity bin is only two, and one of them (SM-z12-1) is located behind a galaxy cluster region where the effect of gravitational lensing needs to be considered.

### 3. SB Profile Fitting

We measure the half-light radii of our high-z galaxy candidates by fitting the Sérsic profile (Sersic 1968) to the observed two-dimensional (2D) SB profiles. The Sérsic profile has the following functional form:

$$\Sigma(r) = \Sigma_e \exp\left(-b_n \left[ \left(\frac{r}{r_e}\right)^{1/n} - 1 \right] \right), \tag{10}$$

where  $\Sigma_e$  is the SB at the half-light radius  $r_e$ , and n is the Sérsic index. The variable  $b_n$  is determined to make  $r_e$  hold half of the total flux inside. For the profile fitting, we use GALFIT version 3 (Peng et al. 2002, 2010), which convolves a galaxy SB profile with a PSF profile and optimizes the fits using the Levenberg–Marquardt algorithm for  $\chi^2$  minimization. The output parameters of GALFIT include the centroid coordinates of a fitted object, its total magnitude, radius along the semimajor axis (a), Sérsic index (n), axis ratio (b/a), and position angle. From the radius along the semimajor axis and the axis ratio, we calculate the circularized half-light radius,  $r_e = a\sqrt{b/a}$ , for each object because it is frequently used for galaxy size measurements in previous studies (e.g., Mosleh et al. 2012; Newman et al. 2012; Ono et al. 2013; Shibuya et al. 2015; Kawamata et al. 2018). We provide the initial parameters used for the GALFIT profile fitting by running SExtractor. All of the parameters, except for the Sérsic index, are allowed to vary during the profile fitting. The Sérsic index

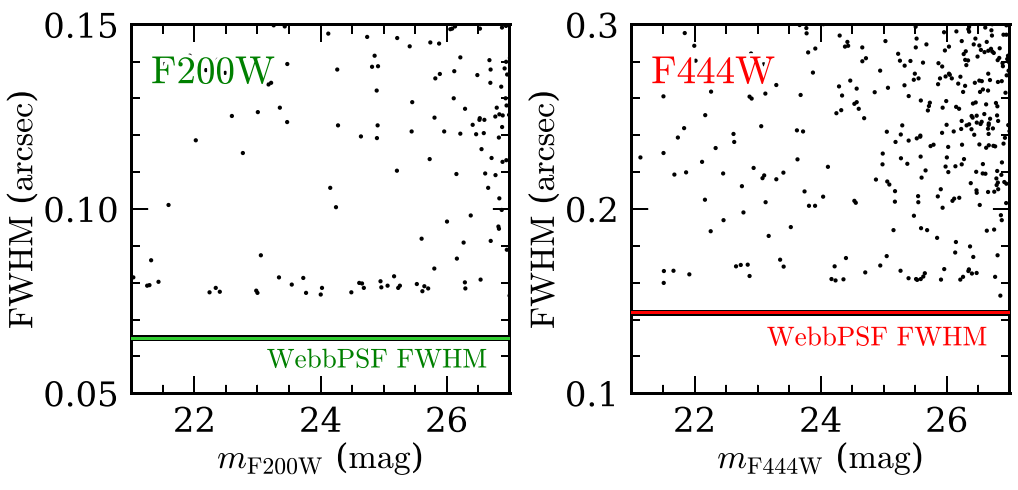


**Figure 2.** Left: FWHM vs. 0."2 diameter aperture magnitude for bright objects with relatively small FWHMs detected in the F200W image for the GLASS field (black dots). The solid horizontal green line represents the FWHM of PSF created with WebbPSF. Note that the PSF created with WebbPSF is not drizzled. Right: same as the left panel but for F444W.

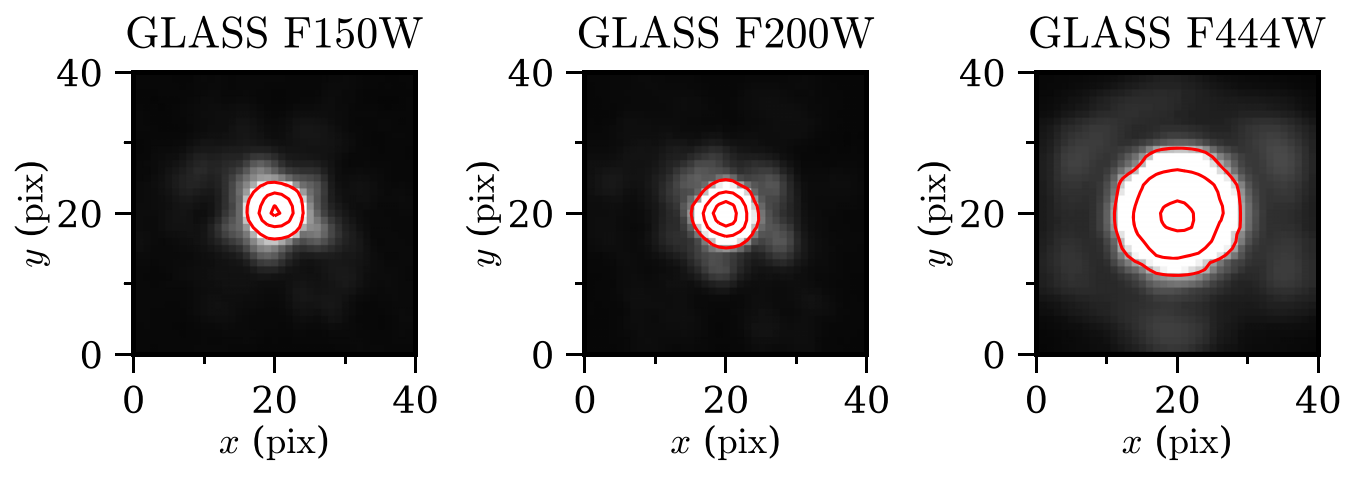


**Figure 3.** Example PSF images in F150W, F200W, and F444W for the GLASS field. The red contours correspond to  $300\sigma$ ,  $1000\sigma$ , and  $2000\sigma$  for F150W and F200W, and  $100\sigma$ ,  $300\sigma$ , and  $700\sigma$  for F444W. The FWHMs of these PSFs are summarized in Table 4.

ID	R.A. (hh:mm:ss)	Decl. (dd:mm:ss)	$z_{ m photo}$	$Z_{ m spec}$	$m_{ m UV}^{ m (ap)}$ (mag)	M <sub>UV</sub> (mag)
(1)	(2)	(3)	(4)	(5)	(flag) (6)	(111ag) (7)
		1	$L/L_{z=3}^* = 0.3-1$			
GL-z12-1	00:13:59.74	-30:19:29.1	$12.28^{+0.08}_{-0.07}$		27.4	-21.0
S5-z12-1	22:36:06.72	+34:00:09.7	$12.58^{+1.23}_{-0.46}$		28.3	-20.2
CR2-z12-1	14:19:46.36	+52:56:32.8	$11.63^{+0.51}_{-0.53}$	$11.44^{+0.09\mathrm{a}}_{-0.08}$	28.5	-19.9
		$L_{/}$	$L_{z=3}^* = 0.12 - 0.3$			
CR2-z12-3	14:19:41.61	+52:55:07.6	$11.66^{+0.69}_{-0.71}$		28.6	-19.2
CR2-z12-2	14:19:42.57	+52:54:42.0	$11.96^{+1.44}_{-0.87}$		28.9	-19.0
CR2-z12-4	14:19:24.86	+52:53:13.9	$12.08^{+2.11}_{-1.25}$		29.4	-19.0
		L/I	$L_{z=3}^* = 0.048 - 0.12$			
SM-z12-1	07:22:32.59	-73:28:33.3	$12.47^{+1.19}_{+0.72}$		29.0	-18.5
CR3-z12-1	14:19:11.11	+52:49:33.6	$11.05^{+2.24}_{-0.47}$		29.5	-18.4

Note. The values presented in this table have been obtained from Harikane et al. (2023). (1) Object ID. (2) R.A. (3) decl. (4) Photometric redshift. (5) Spectroscopic redshift. (6) Aperture magnitude in F200W measured in 0"2 diameter circular aperture. (7) Total absolute UV magnitude.

<sup>a</sup> Obtained by Arrabal Haro et al. (2023).

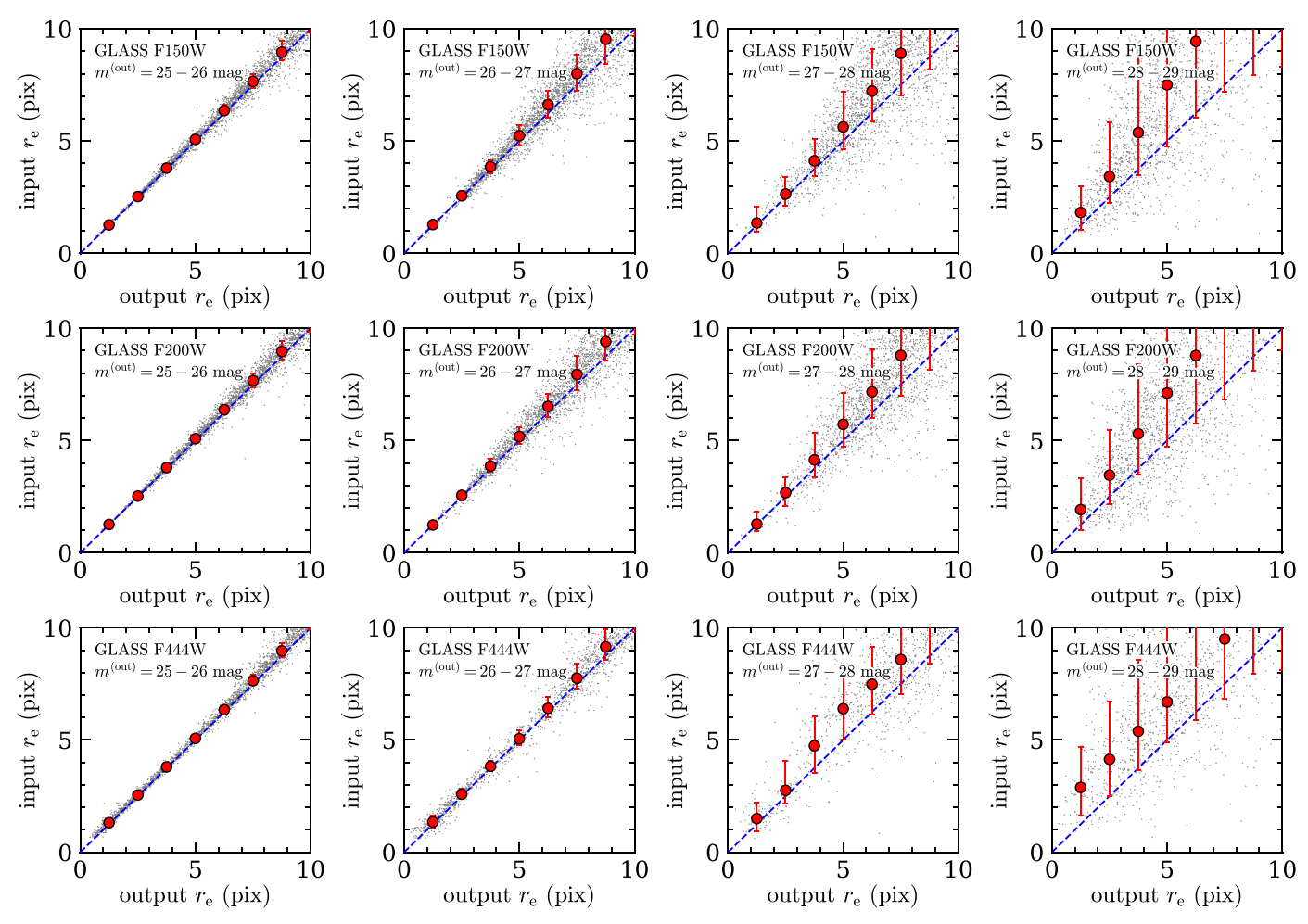


**Figure 4.** Input circularized radius vs. output circularized radius for a range of output total magnitude  $m^{(\text{out})} = 25-26$  mag, 26–27 mag, 27–28 mag, and 28–29 mag from left to right, based on our GALFIT MC simulations. From top to bottom, the results for the GLASS field in F150W, F200W, and F444W are presented. The red-filled circles and the red error bars correspond to the median values of the difference between the input and output magnitudes and the 68 percentile ranges, respectively. The gray dots denote the results for individual simulated objects. The blue-dashed line represents the relation that the input and output circularized radius are equal.

ID (1)	R.A. (hh:mm:ss) (2)	Decl. (dd:mm:ss) (3)	Z <sub>photo</sub> (4)	m <sub>UV</sub> <sup>(ap)</sup> (mag) (5)	M <sub>UV</sub> (mag) (6)
		Stephan's Qui	ntet		
S5-z16-1	22:36:03.81	+33:54:16.7	$16.41^{+0.66}_{-0.55}$	27.6	-21.6

**Note.** The values presented in this table have been obtained from Harikane et al. (2023). (1) Object ID. (2) R.A. (3) decl. (4) Photometric redshift. (5) Aperture magnitude in F277W measured in 0."2 diameter circular aperture. (6) Total absolute UV magnitude.

is fixed at n = 1.5, which corresponds to the median value obtained in previous work with HST for star-forming galaxies (SFGs) with UV luminosities similar to those of our high-z galaxy candidates (Shibuya et al. 2015). To weight individual pixels during the profile fitting, we use noise images that are obtained from the inverse square root of the weight maps. We

also use segmentation images that are produced by SExtractor, for masking objects other than the object we are interested in.

As demonstrated in previous work (e.g., Ono et al. 2013; Shibuya et al. 2015), GALFIT cannot completely trace the outskirts of a galaxy, providing systematically low half-light radii and faint total magnitudes, particularly for faint objects. To quantify and correct for such systematic effects, we conduct the following MC simulations. We use GALFIT to produce galaxy images whose Sérsic index n is fixed at 1.5, <sup>12</sup> half-light radius  $r_e$  is randomly chosen between 0.5 and 27.0 pixels, and total magnitude is randomly chosen between 24.5 and 30.0 mag. We convolve them with a PSF image that is a composite of bright and unsaturated stellar objects in each observed field and each band. The PSF-convolved galaxy images are then inserted into blank regions of the real NIRCam images and

 $<sup>\</sup>overline{11}$  We confirm that our results are almost the same when we fix the Sérsic index at n=1.0.

 $<sup>\</sup>overline{}^{12}$  Although this fixed value corresponds to the median value obtained for SFGs at lower redshifts using the HST data as described above, the Sérsic index is not constrained well for SFGs at high redshifts comparable to those investigated in this study. In Appendix, we present the results of MC simulations with input Sérsic index values ranging from n=0.5-5.0, to demonstrate an extreme case where the Sérsic index has a large scatter, resulting in a large systematic uncertainty. The Sérsic index of high-z galaxies should be well constrained in future studies.

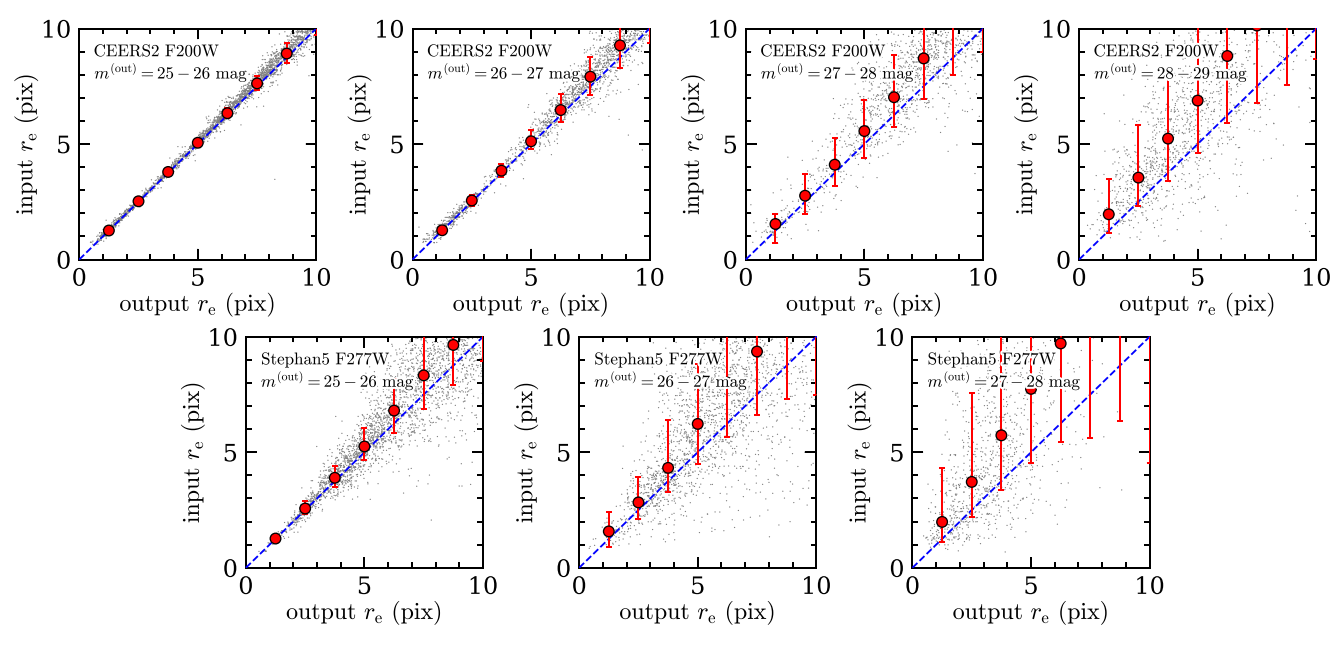


Figure 5. Continuation of Figure 4. From top to bottom, the results for the CEERS2 field in F200W, and Stephan's Quintet field in F277W are presented.

$5\sigma$ Depth / $10\sigma$ Depth / PSF FWHM				
Field	F150W	F200W	F277W	F444W
GLASS	29.4 / 28.6 / 0."0704	29.6 / 28.8 / 0."0776	•••	29.6 / 28.8 / 0."1605
CEERS	•••	29.7 / 28.9 / 0."0795	•••	•••
SMACS J0723		29.6 / 28.8 / 0."0765		
Stephan's Quintet		28.1 / 27.3 / 0."0771	28.8 / 28.0 / 0."1197	

Note. Limiting magnitudes are measured with randomly distributed 0.12 diameter circular apertures (Harikane et al. 2023).

analyzed in the same manner as that for our high-z galaxy candidates.

In Figures 4 and 5, we present the results of size measurements of our MC-simulated galaxies. The panels show the input circularized half-light radius,  $r_e^{(\text{int})}$ , versus the output circularized half-light radius,  $r_e^{(\text{out})}$ , for each image at four different output total magnitude ranges of  $m^{(\text{out})} = 25-26$ , 26-27, 27-28, and 28-29 mag. As expected, we find that measured sizes for all the images show small systematic offsets for objects with small sizes, although the fitting progressively underestimates the sizes at large sizes. The systematic offsets and statistical uncertainties are larger for fainter objects. The median values of input circularized half-light radii as a function of output circularized half-light radius are presented in Table 5.

Figures 6 and 7 show the results of total magnitude measurements at two different output size ranges of  $r_e^{(\text{out})} = 0$ –5 and 5–10 pixels for each image. As expected, it is found that measured total magnitudes show small systematic offsets for objects with relatively bright magnitudes, but they are systematically fainter than the input values for faint objects. The systematic offsets and statistical uncertainties are larger for objects with larger sizes. The median values of input total magnitudes as a function of output total magnitudes are presented in Table 6.

In summary, our MC simulations indicate that GALFIT measurements of half-light radii and total magnitudes are

systematically underestimated for faint objects. We correct for these systematic effects and also estimate statistical uncertainties in size and total magnitude measurements based on our MC simulation results. More specifically, for size measurements, we use the MC simulation results in the output magnitude bins corresponding to the objects we study to correct for the output sizes by the differences between the input and output sizes. Similarly, for total magnitude measurements, we refer to the MC simulation results in the output size bins corresponding to the objects we investigate. We then correct for the output magnitudes by the differences between the input and output magnitudes.

# 4. Results

# 4.1. SB Profile Fitting Results for the Rest-frame UV Continuum

We perform SB profile fitting for our  $z \sim 9-16$  galaxy candidates with GALFIT. We individually measure the sizes of the bright objects, for which the S/Ns of the aperture magnitudes are greater than 10, and extend the measurements to fainter ones by stacking their images. We correct for the systematic effects by using the MC simulation results presented in Section 3.

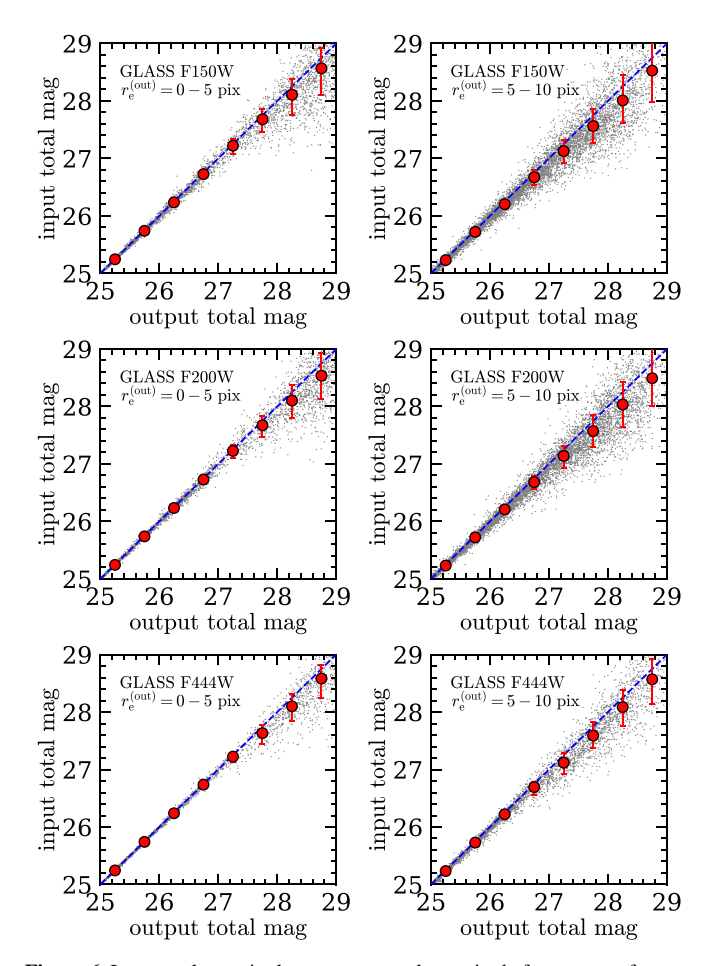
Figure 8 shows the results of the SB profile fitting for the one F115W dropout with S/N > 10, GL-z9-1. The  $1\rlap.{''}5 \times 1\rlap.{''}5$  cutouts of the original image, the best-fit model image, the residual image (i.e., the original image cutout—the best-fit model image), and the segmentation map are presented from

Table 5
Output and Median Input Circularized Radii with 68 Percentile Ranges Based on Our GALFIT MC Simulations

Output r <sub>e</sub>	Input r <sub>e</sub>	Input r <sub>e</sub>	Input r <sub>e</sub>	Input r <sub>e</sub>
	at 25–26 mag	at 26-27 mag	at 27-28 mag	at 28-29 mag
(pix)	(pix)	(pix)	(pix)	(pix)
(1)	(2)	(3)	(4)	(5)
		GLASS F150		
1.25	$1.26^{+0.05}_{-0.05}$	$1.28^{+0.14}_{-0.15}$	$1.35^{+0.72}_{-0.37}$	$1.82^{+1.17}_{-0.77}$
2.50	$2.53^{+0.08}_{-0.07}$	$2.56^{+0.21}_{-0.18}$	$2.64^{+0.76}_{-0.52}$	$3.42^{+2.40}_{-1.18}$
3.75	$3.79^{+0.12}_{-0.10}$	$3.85^{+0.30}_{-0.27}$	$4.12^{+0.96}_{-0.70}$	$5.38^{+3.84}_{-1.91}$
5.00	$5.07^{+0.18}_{-0.17}$	$5.24^{+0.46}_{-0.42}$	$5.63^{+1.55}_{-0.98}$	$7.51^{+4.11}_{-2.76}$
6.25	$6.36^{+0.26}_{-0.22}$	$6.62^{+0.60}_{-0.57}$	$7.23^{+1.86}_{-1.37}$	$9.44^{+4.13}_{-3.38}$
7.50	$7.65^{+0.32}_{-0.29}$	$8.00^{+0.86}_{-0.75}$	$8.91^{+2.45}_{-1.88}$	$11.12^{+4.41}_{-3.92}$
8.75	$8.96^{+0.49}_{-0.38}$	$9.53^{+1.02}_{-1.11}$	$10.51^{+3.06}_{-2.32}$	$12.15^{+4.93}_{-4.19}$
	10.04	GLASS F200		+1.40
1.25	$1.26^{+0.04}_{-0.03}$	$1.24^{+0.11}_{-0.13}$	$1.28^{+0.56}_{-0.31}$	$1.92^{+1.40}_{-0.92}$
2.50	$2.53^{+0.07}_{-0.06}$	$2.56^{+0.20}_{-0.21}$	$2.68^{+0.71}_{-0.60}$	$3.46^{+2.00}_{-1.30}$
3.75	$3.80^{+0.12}_{-0.10}$	$3.87^{+0.31}_{-0.26}$	$4.14^{+1.19}_{-0.76}$	$5.30^{+3.09}_{-1.83}$
5.00	$5.08^{+0.17}_{-0.15}$	$5.18^{+0.42}_{-0.31}$	$5.72^{+1.38}_{-0.99}$	$7.12^{+3.98}_{-2.38}$
6.25	$6.37^{+0.23}_{-0.20}$	$6.52^{+0.56}_{-0.46}$	$7.17^{+1.91}_{-1.17}$	$8.79^{+4.68}_{-3.01}$
7.50	$7.67^{+0.33}_{-0.28}$	$7.94^{+0.81}_{-0.69}$	$8.80^{+2.32}_{-1.78}$	$10.53^{+4.89}_{-3.68}$
8.75	$8.97^{+0.45}_{-0.38}$	$9.41^{+0.97}_{-0.86}$	$10.55^{+2.59}_{-2.41}$	$12.02^{+4.72}_{-3.92}$
	+0.13	GLASS F444		• aa±1 80
1.25	$1.32^{+0.13}_{-0.10}$	$1.35^{+0.28}_{-0.24}$	$1.50^{+0.72}_{-0.56}$	$2.89^{+1.80}_{-1.24}$
2.50	$2.55^{+0.12}_{-0.09}$	$2.59^{+0.24}_{-0.22}$	$2.76^{+1.30}_{-0.60}$	$4.14^{+2.59}_{-1.63}$
3.75	$3.80^{+0.12}_{-0.09}$	$3.83^{+0.23}_{-0.21}$	$4.75^{+1.31}_{-1.22}$	$5.39^{+3.17}_{-1.74}$
5.00	$5.07^{+0.15}_{-0.11}$	$5.06^{+0.37}_{-0.29}$	$6.39^{+1.53}_{-1.38}$	$6.70^{+3.83}_{-1.80}$
6.25	$6.35^{+0.21}_{-0.14}$	$6.41^{+0.50}_{-0.38}$	$7.48^{+1.67}_{-1.34}$	$7.98^{+3.98}_{-2.08}$
7.50	$7.64^{+0.27}_{-0.19}$	$7.75^{+0.65}_{-0.47}$	$8.59^{+1.85}_{-1.53}$	$9.50^{+3.48}_{-2.67}$
8.75	$8.97^{+0.35}_{-0.28}$	9.15 <sup>+0.79</sup> <sub>-0.59</sub>	$10.32^{+2.31}_{-1.92}$	$11.26^{+4.36}_{-3.32}$
1.25	$1.26^{+0.05}_{-0.07}$	CEERS2 F200 1.27 <sup>+0.09</sup> <sub>-0.17</sub>	1.54 <sup>+0.45</sup> <sub>-0.84</sub>	$1.96^{+1.51}_{-0.82}$
1.25 2.50	$2.52^{+0.09}_{-0.08}$	$1.27_{-0.17}$ $2.55_{-0.22}^{+0.25}$	1.54 <sub>-0.84</sub> 2.76+0.94	$3.55^{+2.29}_{-1.24}$
3.75	$3.79^{+0.13}_{-0.11}$	2.33 <sub>-0.22</sub> 2.95+0.27	$2.76^{+0.94}_{-0.78}$ $4.10^{+1.15}_{-0.94}$	5.23 <sup>+2.99</sup> <sub>-1.85</sub>
5.00	$5.79_{-0.11}$ $5.05_{-0.18}^{+0.18}$	$3.85^{+0.27}_{-0.28}$ $5.12^{+0.47}_{-0.34}$	$5.56^{+1.36}_{-1.15}$	$6.88^{+4.05}_{-2.25}$
6.25	$6.33^{+0.23}_{-0.22}$	$6.47^{+0.69}_{-0.51}$	$7.03^{+1.84}_{-1.30}$	8.81 <sup>+3.88</sup> <sub>-2.91</sub>
7.50	$7.62^{+0.31}_{-0.30}$	$0.47_{-0.51}$	$8.70^{+2.41}_{-1.74}$	$10.13^{+3.76}_{-3.37}$
8.75	$8.92^{+0.46}_{-0.43}$	$7.91^{+0.85}_{-0.80}$	$10.28^{+2.71}_{-2.28}$	$10.13_{-3.37}$ $11.07_{-3.51}^{+4.70}$
6.73		9.27 <sup>+1.09</sup> <sub>-0.99</sub> Stephan's Quintet		11.07_3.51
1.25	$1.26^{+0.15}_{-0.17}$	$1.57^{+0.83}_{-0.66}$	$1.98^{+2.34}_{-0.87}$	
2.50	$2.56^{+0.34}_{-0.22}$	$2.83^{+1.08}_{-0.71}$	$3.72^{+3.84}_{-1.53}$	
3.75	$3.89^{+0.52}_{-0.40}$	$4.32^{+2.07}_{-1.05}$	$5.72_{-1.53}^{+4.40}$ $5.73_{-2.39}^{+4.40}$	
5.00	$5.05_{-0.40}^{+0.80}$ $5.25_{-0.60}^{+0.80}$	$6.23^{+2.59}_{-1.74}$	$7.74^{+5.11}_{-3.20}$	
6.25	$6.80^{+1.35}_{-0.96}$	$8.01^{+3.20}_{-2.37}$	$9.71^{+5.58}_{-4.26}$	
7.50	$8.33^{+1.77}_{-1.47}$	$9.36^{+4.22}_{-2.75}$	$11.21^{+6.52}_{-5.61}$	•••
8.75	$9.65^{+2.08}_{-1.74}$	$10.93^{+4.39}_{-3.64}$	$11.21_{-5.61}$ $11.07_{-4.72}^{+9.52}$	
0.75	J.03 <sub>-1.74</sub>	10.23_3.64	11.07-4.72	

**Note.** (1) Output circularized radii. (2)–(5) Median input circularized radii for a range of output total magnitudes  $m^{(\text{out})}=25$ –26 mag, 26–27 mag, 27–28 mag, and 28–29 mag, respectively.

left to right. The best-fit parameters of the total magnitudes and the circularized half-light radii are summarized in Table 7, where the systematic effects and statistical uncertainties are taken into account based on our MC simulation results. Although the total magnitude of GL-z9-1, whose photo-z is relatively high, may be underestimated in F150W due to the Lyman break, we confirm that its total magnitude in F200W is almost the same by performing the profile fitting with the F200W image.



**Figure 6.** Input total magnitude vs. output total magnitude for a range of output half-light radii  $r_{\rm c}^{\rm (out)}=0$ –5 pixels (left) and 5–10 pixels (right) based on our GALFIT MC simulations. From top to bottom, the results for the GLASS field in F150W, F200W, and F444W are presented. The red-filled circles and the red error bars correspond to the median values of the difference between the input and output magnitudes and the 68 percentile ranges, respectively. The gray dots denote the results for individual simulated objects. The blue-dashed line represents the relation that the input and output magnitudes are equal.

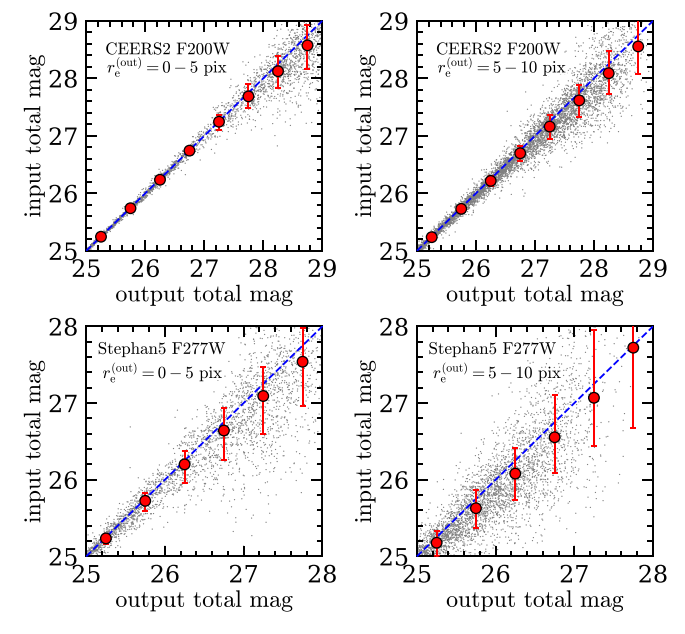


**Figure 7.** Continuation of Figure 6. From top to bottom, the results for the CEERS2 field in F200W, and Stephan's Quintet field in F277W are presented.

Table 6
Output and Median Input Total Magnitudes with 68 Percentile Ranges Based on Our GALFIT MC Simulations

Output Total mag	Input Total mag	Input Total mag
	at 0–5 pix	at 5–10 pix
(mag)	(mag)	(mag)
(1)	(2)	(3)
	GLASS F150W	.0.03
25.25	$25.24_{-0.02}^{+0.02}$	$25.23^{+0.03}_{-0.04}$
25.75	$25.74^{+0.03}_{-0.03}$	$25.72^{+0.05}_{-0.06}$
26.25	$26.24_{-0.05}^{+0.04}$	$26.20^{+0.08}_{-0.09}$
26.75	$26.73_{-0.07}^{+0.07}$	$26.67^{+0.12}_{-0.14}$
27.25	$27.22^{+0.12}_{-0.14}$	$27.13^{+0.20}_{-0.21}$
27.75	$27.68^{+0.18}_{-0.22}$	$27.56^{+0.30}_{-0.29}$
28.25	$28.11^{+0.27}_{-0.35}$	$28.01^{+0.44}_{-0.40}$
28.75	$28.57^{+0.36}_{-0.47}$	$28.53^{+0.57}_{-0.55}$
	GLASS F200W	
25.25	$25.24^{+0.01}_{-0.02}$	$25.23^{+0.03}_{-0.03}$
25.75	$25.74^{+0.02}_{-0.03}$	$25.72^{+0.04}_{-0.05}$
26.25	$26.23^{+0.04}_{-0.04}$	$26.21^{+0.06}_{-0.08}$
26.75	$26.73_{-0.06}^{+0.07}$	$26.68^{+0.11}_{-0.12}$
27.25	$27.23^{+0.10}_{-0.12}$	$27.14^{+0.18}_{-0.20}$
27.75	$27.67^{+0.17}_{-0.21}$	$27.57^{+0.28}_{-0.28}$
28.25	$28.10_{-0.31}^{+0.27}$	$28.03_{-0.39}^{+0.40}$
28.75	$28.53^{+0.39}_{-0.41}$	$28.49_{-0.48}^{+0.59}$
	GLASS F444W	-0.48
25.25	$25.24^{+0.01}_{-0.01}$	$25.23^{+0.02}_{-0.03}$
25.75	$25.74^{+0.01}_{-0.02}$	$25.73^{+0.03}_{-0.04}$
26.25	$26.24^{+0.02}_{-0.02}$	$26.22^{+0.05}_{-0.06}$
26.75	$26.74^{+0.04}_{-0.04}$	$26.69^{+0.09}_{-0.13}$
27.25	$27.22^{+0.06}_{-0.10}$	$27.12^{+0.17}_{-0.19}$
27.75	$27.63^{+0.15}_{-0.18}$	$27.59^{+0.23}_{-0.22}$
28.25	$28.10^{+0.21}_{-0.25}$	$28.09^{+0.29}_{-0.32}$
28.75	$28.58^{+0.24}_{-0.33}$	$28.57_{-0.43}^{+0.36}$
26.73	CEERS2 F200W	26.57 _0.43
25.25	25.25 <sup>+0.02</sup> <sub>-0.02</sub>	$25.24_{-0.03}^{+0.03}$
25.75	$25.23_{-0.02} 25.74_{-0.03}^{+0.03}$	$25.73^{+0.05}_{-0.06}$
26.25	$26.24^{+0.03}_{-0.04}$	$26.22^{+0.08}_{-0.09}$
	26.24 <sub>-0.04</sub>	26.22 <sub>-0.09</sub> 26.70 <sup>+0.13</sup>
26.75	$26.74^{+0.06}_{-0.06}$	$26.70^{+0.13}_{-0.13}$
27.25	$27.25^{+0.12}_{-0.14}$	$27.16^{+0.20}_{-0.21}$
27.75	$27.69^{+0.21}_{-0.21}$	$27.62^{+0.27}_{-0.28}$
28.25	$28.12^{+0.27}_{-0.29}$	$28.09^{+0.39}_{-0.36}$
28.75	28.57 <sup>+0.35</sup> <sub>-0.42</sub>	$28.56^{+0.53}_{-0.47}$
25.25	Stephan's Quintet F277W	25.10+0.15
25.25	25.23 <sup>+0.06</sup> 25.72 <sup>+0.11</sup>	$25.18^{+0.15}_{-0.17}$
25.75	$25.72^{+0.11}_{-0.13}$	25.63 <sup>+0.23</sup> <sub>-0.26</sub>
26.25	$26.20^{+0.18}_{-0.24}$	$26.08^{+0.34}_{-0.34}$
26.75	$26.64^{+0.30}_{-0.38}$	$26.55^{+0.56}_{-0.47}$
27.25	$27.09^{+0.37}_{-0.50}$	$27.07^{+0.89}_{-0.63}$
27.75	$27.54^{+0.44}_{-0.58}$	$27.72^{+1.23}_{-1.05}$

**Note.** (1) Output total magnitude. (2)–(3) Median input total magnitude for a range of output half-light radii  $r_{\rm e}^{\rm (out)}=0$ –5 pixels and 5–10 pixels, respectively.

Similarly, Figures 9 and 10 present the results of the SB profile fitting for the four F150W dropouts with S/N > 10, GLz12-1, CR2-z12-1, CR2-z12-2, and CR2-z12-3, and the one F200W dropout with S/N > 10, S5-z16-1, respectively. Their best-fit total magnitudes and half-light radii are summarized in Tables 8 and 9.

GL-z9-1









**Figure 8.** Sérsic profile fitting results for bright F150W dropouts ( $z \sim 9$  galaxy candidates). From left to right, the  $1\rlap.{''}5 \times 1\rlap.{''}5$  cutouts of the original image, the best-fit Sérsic model profile images, the residual images that are made by subtracting the best-fit images from the original ones, and the segmentation maps used for masking all the neighboring objects during the profile fitting are presented.

The SB profile fittings for two bright candidates in our samples (GL-z9-1 and GL-z12-1) have also been conducted in other studies. Their sizes and total magnitudes are summarized in Table 10 and compared with our results in Figure 11. Yang et al. (2022) performed the SB profile fittings for GL-z9-1 and GL-z12-1 with Galight (Ding et al. 2020). Our size and total magnitude measurement results are broadly consistent with their results although they fix the Sérsic index at n = 1.0, which is slightly different from our fixed value. For GL-z12-1, Naidu et al. (2022a) also presented size measurement results by using GALFIT. Their obtained magnitude is roughly consistent, but the obtained size is much larger than our results. A possible reason for this discrepancy is that they use a different filter image. They use F444W, while we use F200W. However, if we use the F444W image, we still obtain a smaller size than their result. Another potential factor contributing to the difference is that they allow the Sérsic index to vary as a free parameter in their fitting, resulting in a slightly different best-fit value (n = 1.0) compared to our fixed value. However, when we perform the fitting with a fixed Sérsic index value of n = 1.0, the best-fit size is almost the same with only a marginal increase of about 10%. 13 Another possible reason is that they use theoretical PSF models generated with WebbPSF. This discrepancy may be due to their use of a PSF created with WebbPSF that deviates slightly from the actual PSF, resulting in their large  $r_{\rm e}$  (See Section 2).

In Figure 12, we show the SB profile fitting results for the stacked F115W dropouts, whose UV luminosities are  $L/L_{z=3}^* = 0.12$ –0.3 and 0.048–0.12, as well as the stacked F150W dropout with UV luminosities  $L/L_{z=3}^* = 0.12$ –0.3. Because the axis ratios of the stacked objects should be close to unity, the axis ratio and position angle are fixed at 1 and 0, respectively. The best-fit parameters of the SB profile fitting for the stacked objects are also presented in Tables 7 and 8, where the systematic effects and statistical uncertainties in the size and total magnitude measurements are considered based on our MC simulation results.

In summary, our size measurement results indicate that most of the  $z\sim9$ –16 galaxy candidates have small sizes of around 200–500 pc, which is comparable to previous results based on deep HST data for high-z galaxies with similar UV luminosities (e.g., Ono et al. 2013; Kawamata et al. 2015; Shibuya et al. 2015). Interestingly, in our samples, GL-z12-1 is exceptionally compact with a half-light radius of only  $39\pm11$  pc. We discuss its physical origin in Section 5.

 $<sup>\</sup>overline{^{13}}$  Although we also attempt the SB fitting with the Sérsic index as a free parameter, we encounter convergence issues with GALFIT in that case.

<sup>&</sup>lt;sup>14</sup> Because the number of F150W dropouts with  $L/L_{z=3}^* = 0.12-0.3$  is small, we also perform the profile fitting with the axis ratio and position angle free, and confirm that the results are almost the same.

Table 7
SB Profile Fitting Results for  $z \sim 9$  Galaxy Candidates (F115W Dropouts)

ID (1)	m <sub>UV</sub> (mag) (2)	M <sub>UV</sub> (mag) (3)	r <sub>e</sub> (kpc) (4)	m <sub>opt</sub> (mag) (5)	M <sub>opt</sub> (mag) (6)	r <sub>e,opt</sub> (kpc) (7)
GL-z9-1	$26.82^{+0.07}_{-0.07}$	$-20.72^{+0.07}_{-0.07}$	$L/L_{z=3}^* = 0.3-1$ $0.30_{-0.02}^{+0.03}$	$26.30_{-0.02}^{+0.02}$	$-21.25^{+0.02}_{-0.02}$	$0.28^{+0.02}_{-0.01}$
z9-stack-1	$28.21^{+0.20}_{-0.21}$	$-19.12^{+0.20}_{-0.21}$	$L/L_{z=3}^* = 0.12-0.3$ $0.49_{-0.09}^{+0.14}$	$27.89^{+0.09}_{-0.13}$	$-19.43^{+0.09}_{-0.13}$	$0.71^{+0.16}_{-0.12}$
z9- stack-2	$28.67^{+0.12}_{-0.14}$	$-18.65^{+0.12}_{-0.14}$	$L/L_{z=3}^* = 0.048-0.12$ $0.29_{-0.06}^{+0.09}$	28.99 <sup>+0.15</sup> <sub>-0.18</sub>	$-18.34^{+0.15}_{-0.18}$	$0.24^{+0.15}_{-0.10}$

**Note.** The systematic effects and statistical uncertainties in these obtained size and total magnitude measurements are considered based on our MC simulation results. (1) Object ID. (2) Total apparent UV magnitude measured by GALFIT. (3) Total absolute UV magnitude using  $z_{\text{photo}}$ . For the stacked objects, we use  $z_{\text{photo}} = 9.0$ . (4) UV circularized half-light radius  $r_{\text{e}} = a\sqrt{b/a}$ , where a is the radius along the semimajor axis and b/a is the axis ratio. (5) Total apparent optical magnitude measured by GALFIT. (6) Total absolute optical magnitude using  $z_{\text{photo}}$ . For the stacked objects, we use  $z_{\text{photo}} = 9.0$ . (7) Optical circularized half-light radius.

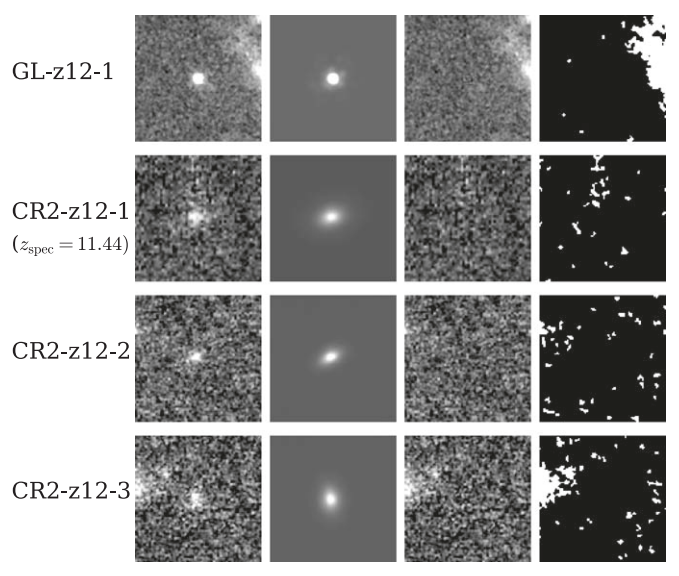


**Figure 9.** Same as Figure 8, but for bright F200W dropouts ( $z \sim 12$  galaxy candidates).

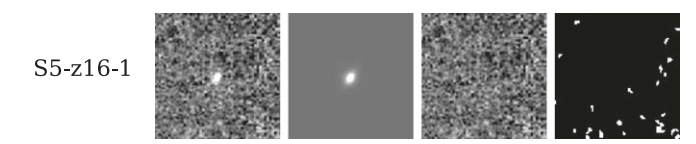


Figure 10. Same as Figure 8, but for bright F277W dropouts ( $z \sim 16$  galaxy candidates).

# 4.2. SB Profile Fitting Results for the Rest-frame Optical Continuum

For  $z\sim 9$  galaxy candidates, we perform the SB profile fitting with the F444W images to obtain their sizes and total magnitudes in the rest-frame optical in the same manner as in the rest-frame UV. In Figure 13, we present the results of the profile fitting for GL-z9-1, which is the only object in our sample showing an S/N >10 in F444W. In the same figure, we also show the profile fitting results for the stacked F115W dropouts, whose UV luminosities are  $L/L_{z=3}^*=0.12$ –0.3 and 0.048–0.12. Their best-fit parameters of the profile fitting are also presented in Table 7.

The rest-frame optical continuum profile fitting for GL-z9-1 has also been carried out in previous work as presented in

ID (1)	m <sub>UV</sub> (mag)	M <sub>UV</sub> (mag)	r <sub>e</sub> (kpc)
(1)	(2)	(3)	(4)
	$L/L_{z=3}^*$ =	= 0.3-1	
GL-z12-1	$26.90^{+0.07}_{-0.06}$	$-20.87^{+0.07}_{-0.06}$	$0.04^{+0.01}_{-0.01}$
CR2-z12-1	$27.22^{+0.20}_{-0.21}$	$-20.45^{+0.20}_{-0.21}$	$0.36^{+0.08}_{-0.06}$
	$L/L_{z=3}^* =$	0.12-0.3	
CR2-z12-2	$27.86^{+0.21}_{-0.21}$	$-19.88^{+0.21}_{-0.21}$	$0.18^{+0.05}_{-0.04}$
CR2-z12-3	$27.59^{+0.12}_{-0.14}$	$-20.11^{+0.12}_{-0.14}$	$0.28^{+0.08}_{-0.06}$
z12-stack-1	$28.13^{+0.12}_{-0.14}$	$-19.61^{+0.12}_{-0.14}$	$0.20^{+0.05}_{-0.04}$

**Note.** The systematic effects and statistical uncertainties in these obtained size and total magnitude measurements are considered based on our MC simulation results. (1) Object ID. (2) Total apparent UV magnitude measured by GALFIT. (3) Total absolute UV magnitude using  $z_{\rm photo}$ . For the stacked objects, we use  $z_{\rm photo} = 12.0$ . (4) Circularized half-light radius  $r_{\rm e} = a\sqrt{b/a}$ .

Table 9 SB Profile Fitting Results for  $z \sim 16$  Galaxy Candidates (F200W Dropouts)

ID	$m_{ m UV}$	$M_{ m UV}$	$r_{\rm e}$
(1)	(mag) (2)	(mag) (3)	(kpc) (4)
S5-z16-1	$26.56^{+0.18}_{-0.24}$	$-21.62^{+0.18}_{-0.24}$	$0.15^{+0.09}_{-0.06}$

**Note.** The systematic effects and statistical uncertainties in these obtained size and total magnitude measurements are considered based on our MC simulation results. (1) Object ID. (2) Total apparent UV magnitude measured by GALFIT. (3) Total absolute UV magnitude using  $z_{\rm photo}$ . (4) Circularized half-light radius  $r_{\rm e}=a\sqrt{b/a}$ .

Table 10 (see also Figure 14). Although our obtained size is smaller than that in Yang et al. (2022), our obtained total magnitude is in good agreement with their result. Naidu et al. (2022a) also performed the profile fitting for GL-z9-1. Although their estimated size is much larger than our result, their obtained total magnitude is broadly consistent with our obtained value. A possible reason for the obtained size difference is the PSF difference as described above. Another possible reason is that the Sérsic index is a free parameter in

GL-z12-1

5153

GL-z12

F200W

F200W

F444W

Reference

(9)

Yang et al. (2022) Naidu et al. (2022a)

Yang et al. (2022)

Naidu et al. (2022a)

This study

This study

ID Filter<sub>UV</sub> **PSF**  $M_{\rm UV}$ Filter<sub>opt</sub>  $M_{\rm opt}$  $r_{\rm e,opt}$ (mag) (kpc) (mag) (kpc) (1) (2) (3) (4) (5) (6) (7) (8) GL-z9-1 F150W  $-20.72^{+0.07}_{-0.07}$  $0.30^{+0.03}_{-0.02}$ F444W  $-21.25^{+0.02}_{-0.02}$  $0.28^{+0.02}_{-0.01}$ **Empirical** F150W F444W 560  $-20.6 \pm 0.20$  $0.37\pm0.03$  $-21.2 \pm 0.05$  $0.50\pm0.02$ **Empirical** GL-z10 F444W  $-20.7 \pm 0.2$ WebbPSF 0.7

 $0.04^{+0.01}_{-0.01}$ 

 $0.12 \pm 0.01$ 

0.5

Table 10
Comparison of Our Profile Fitting Results with Previous Results

Note. (1) Object ID. (2) Filter used for the rest-frame UV continuum profile fitting. (3) Total absolute UV magnitude. (4) Half-light radius in the rest-frame UV. (2) Filter used for the rest-frame optical continuum profile fitting. (6) Total absolute optical magnitude. (7) Half-light radius in the rest-frame optical. (8) Method adopted in making PSFs. (9) Reference.

. . .

their profile fitting, although the best-fit Sérsic index value (n = 0.8 for GL-z9-1) is a disk-like value.

 $-20.87^{+0.07}_{-0.06}$ 

 $-21.1\pm0.1$ 

 $-21.0\pm0.1$ 

Figure 15 presents the size ratio of our  $z \sim 9$  galaxy candidates between the rest-frame UV and optical as a function of  $M_{\rm UV}$ . We also plot the results of Yang et al. (2022) because they examined the size ratios for high-z galaxies down to slightly lower redshifts with JWST. Yang et al. (2022) reported that their  $z \sim 7-9$  galaxy candidates have  $1.32 \pm 0.42$  times larger sizes in the rest-frame optical than in the rest-frame UV. Although their size ratio is consistent with unity within  $1\sigma$ uncertainties, if the size ratio is larger than unity, it would indicate that relatively old stars in  $z \sim 7-9$  bright galaxies already have disk-like structures, and their ongoing star formation is occurring in smaller regions around their center. Note that, in the case of these galaxies containing a considerable amount of dust, their size ratio may be explained by dust because the UV emission is relatively strongly absorbed. However, most of our candidates show blue UV slopes (i.e., F150W-F277W < 0, see Table 3 of Harikane et al. 2023), suggesting that dust extinction is not very effective in these galaxies. Accurate measurements of their dust extinction can be obtained from the flux ratios of the Balmer emission lines by spectroscopy in the future.

Thanks to the stacking analysis, we investigate the size ratio down to a fainter magnitude range compared to the individual analyses. We find that the average size ratio is  $r_{\rm e,opt}/r_{\rm e}=1.16\pm0.31$  for our stacked  $z\sim9$  galaxy candidates with the faint luminosity bins of  $L/L_{z=3}^*=0.12$ –0.3 and 0.048–0.12. Although our results for the faint stacked objects are consistent with those for brighter objects within the  $1\sigma$  uncertainties, if the size ratio for the faint galaxies is smaller than that for the bright ones, it may indicate that the distributions of young massive and old less massive stars are not very different probably because of more recent star formation activities in faint galaxies. This point needs to be investigated for larger samples in future studies.

# 4.3. Size-UV Luminosity Relation

We investigate the size–luminosity ( $r_{\rm e}$ – $L_{\rm UV}$ ) relation for our high-z galaxy candidates. The top panel of Figure 16 presents the size–luminosity relation for our  $z\sim9$  galaxy candidates. The  $z\sim9$  data points are broadly consistent with the previous results for  $z\sim8$  galaxies within  $1\sigma$  uncertainties. Our results for  $z\sim12$ –16 are also presented, although the UV magnitude

ranges that can be examined with the current samples are limited.

. . .

Empirical

Empirical

WebbPSF

Following the previous work, we fit a power-law function to the data points,

$$r_{\rm e} = r_0 \left(\frac{L_{\rm UV}}{L_0}\right)^{\alpha},\tag{11}$$

where  $r_0$  is the effective radius at the luminosity of  $L_0$ , corresponding to -21.0 mag (Huang et al. 2013; Shibuya et al. 2015), and  $\alpha$  is the slope of the size–luminosity relation. Since the previous work has shown that the slope value is almost constant,  $\alpha = 0.27 \pm 0.01$ , over a wide redshift range of z = 0–8 (Shibuya et al. 2015), we fix it at this value and perform the fitting with  $r_0$  as the only free parameter. As a result, we obtain  $r_0 = 0.35 \pm 0.02$  kpc, which is broadly consistent with the best-fit function of  $r_0 \propto (1 + z)^{\beta_z}$  presented in Figure 10 of Shibuya et al. (2015).

We also fit the size–luminosity relation in the same manner to the  $z \sim 12$  data points, although the observed range of UV magnitudes is limited. Note that the data point of GL-z12-1 with the exceptionally small size is not used for the fitting. The obtained  $r_0$  value is  $r_0 = 0.32 \pm 0.03$  kpc, which is also consistent with the extrapolation of the best-fit function of Shibuya et al. (2015).

In addition to the UV luminosity, the relation between stellar mass and size is also interesting for comparison with previous results. In the bottom panel of Figure 16, we show our bright  $z \sim 9-16$  galaxy candidates whose stellar masses can be estimated. The stellar masses for our bright high-z galaxy candidates are estimated with the flexible Bayesian inference spectral energy distribution (SED) fitting code PROSPECTOR (Johnson et al. 2021; for details, see Section 3.3 of Harikane et al. 2023). The stellar masses of our stacked objects are calculated with the stellar mass-to-luminosity ratios of the bright candidates in the same dropout samples. We also plot lower-z SFGs including local objects investigated in the literature. We find that our  $z \sim 9-16$  galaxy candidates have similar sizes and stellar masses to those of  $z \sim 6$  SFGs (Shibuya et al. 2015; Kikuchihara et al. 2020) and local ultracompact dwarfs (UCDs; Norris et al. 2014).

### 4.4. Size Evolution

Previous studies have shown that the galaxy size evolution can be characterized with a functional form of  $r_e \propto (1+z)^s$ 

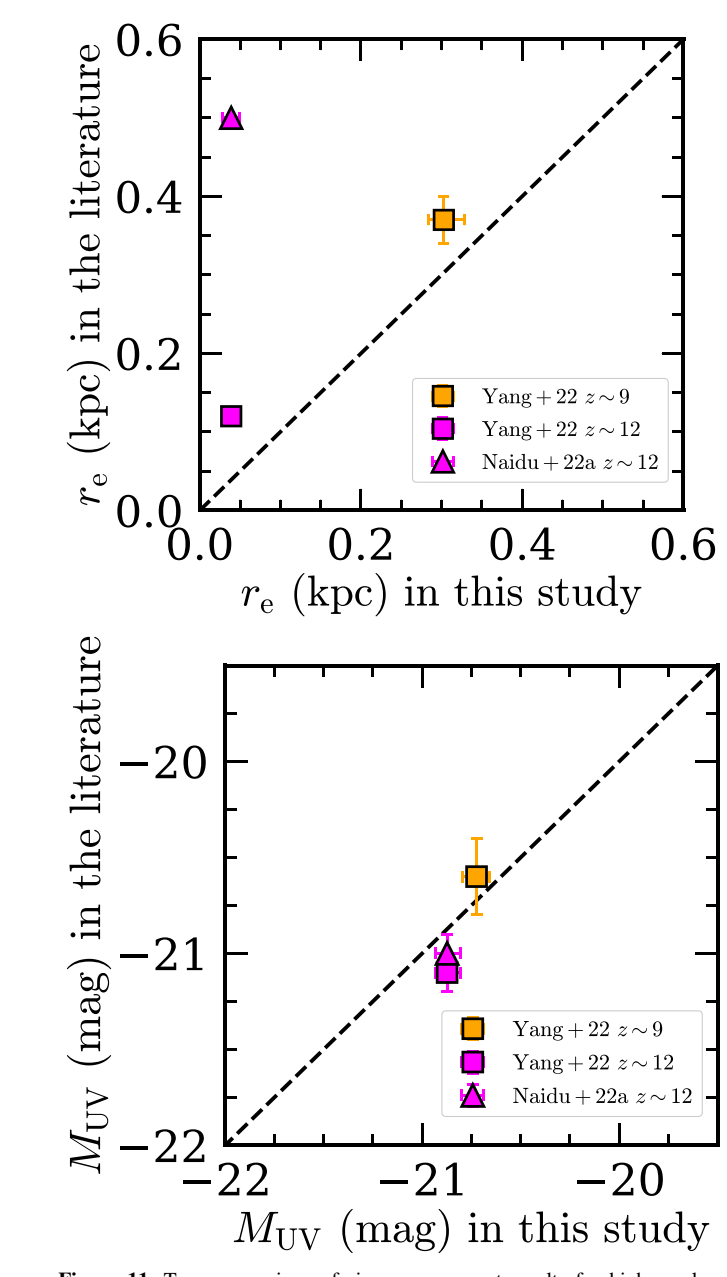


**Figure 11.** Top: comparison of size measurement results for high-z galaxy candidates on an individual basis in the rest-frame UV. The horizontal axis denotes our size measurements and the vertical axis represents those in the literature. The orange square compares our results for the bright  $z \sim 9$  galaxy candidate with those in Yang et al. (2022). The magenta square and triangle show comparisons of our results for the bright galaxy candidate at  $z \sim 12$  with those in Yang et al. (2022) and Naidu et al. (2022a), respectively. The black-dashed line corresponds to the cases where our estimates and those in the literature are equal. Bottom: same as the top panel, but for total absolute magnitudes in the rest-frame UV.

(e.g., Bouwens et al. 2004, 2006; Ferguson et al. 2004; Hathi et al. 2008; Oesch et al. 2010; Ono et al. 2013; Kawamata et al. 2015; Holwerda et al. 2015, 2020; Shibuya et al. 2015; Curtis-Lake et al. 2016; Allen et al. 2017; Kawamata et al. 2018; Bridge et al. 2019), where *s* is the slope of the size evolution. Here we extend the previous work by adding the new JWST measurement results. Following the previous work because of the size dependence on the luminosity, we compare the half-light radii of our high-*z* galaxy candidates within fixed magnitude ranges. In Figure 17, we present the half-light radii

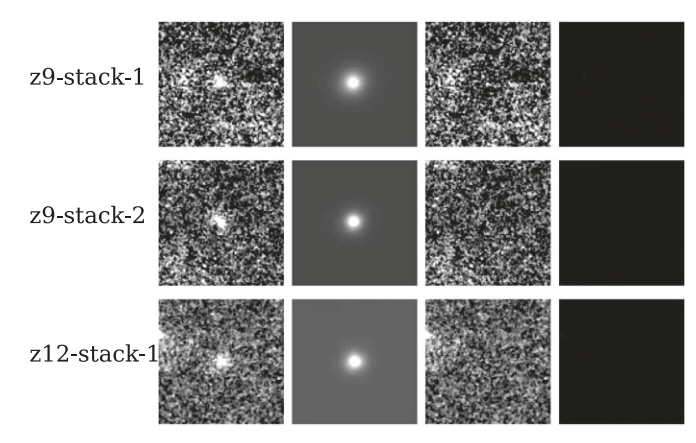


**Figure 12.** Same as Figure 10, except that the objects are stacked F115W dropouts and F150W dropouts.

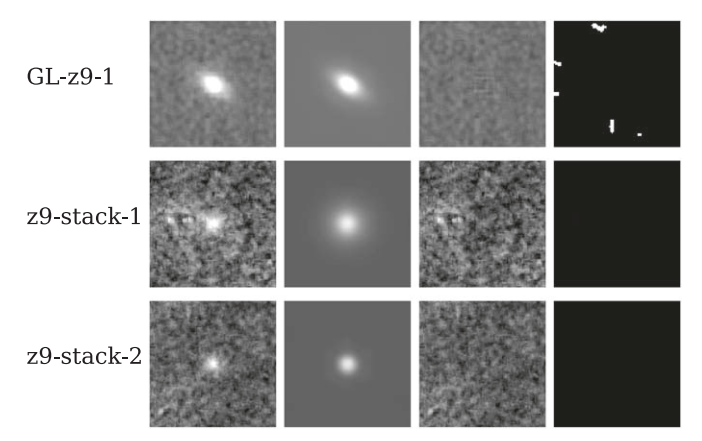


**Figure 13.** Same as Figure 8, but in F444W for GL-z9-1 and the stacked F115W dropouts.

as a function of redshift for our high-z galaxy candidates with  $L/L_{z=3}^*=0.3$ –1 and 0.12–0.3, as well as the HST results for the z=0–8 SFGs presented in Shibuya et al. (2015) and the JWST results for z=9–12 galaxy candidates reported in Yang et al. (2022) and Naidu et al. (2022a).

Since the number of galaxies whose sizes are measured with JWST is limited compared to the previous HST studies, we first compare our results with the extrapolations of the size evolution based on the previous HST results. As can be seen from the top panel of Figure 17, for  $L/L_{7=3}^* = 0.3-1$ , our results at  $z \sim 10$ –16 are broadly consistent with the extrapolation of the HST results within  $1\sigma$  uncertainties. Based on size measurement results up to higher redshifts with JWST, we find that the size evolution of galaxies with  $L/L_{z=3}^* = 0.3-1$  shows almost the same trend beyond z > 10. For the fainter luminosity bin of  $L/L_{r=3}^* = 0.12 - 0.3$ , as shown in the bottom panel of Figure 17, the sizes of the stacked objects of  $z \sim 9$  and  $z \sim 12$ galaxy candidates are also roughly consistent with the extrapolations of the best-fit function obtained in the previous work (solid curve). Note that GL-z12-1 at  $z \sim 12$  has an exceptionally compact size compared to the other candidates at similar redshifts and the extrapolation of the HST results. We discuss possible physical interpretations of its very compact size in Section 5.

Next, although the number of our high-z galaxy candidates with size measurements available is small, we fit the functional form of  $r_e \propto (1+z)^s$  to the data points by taking into account

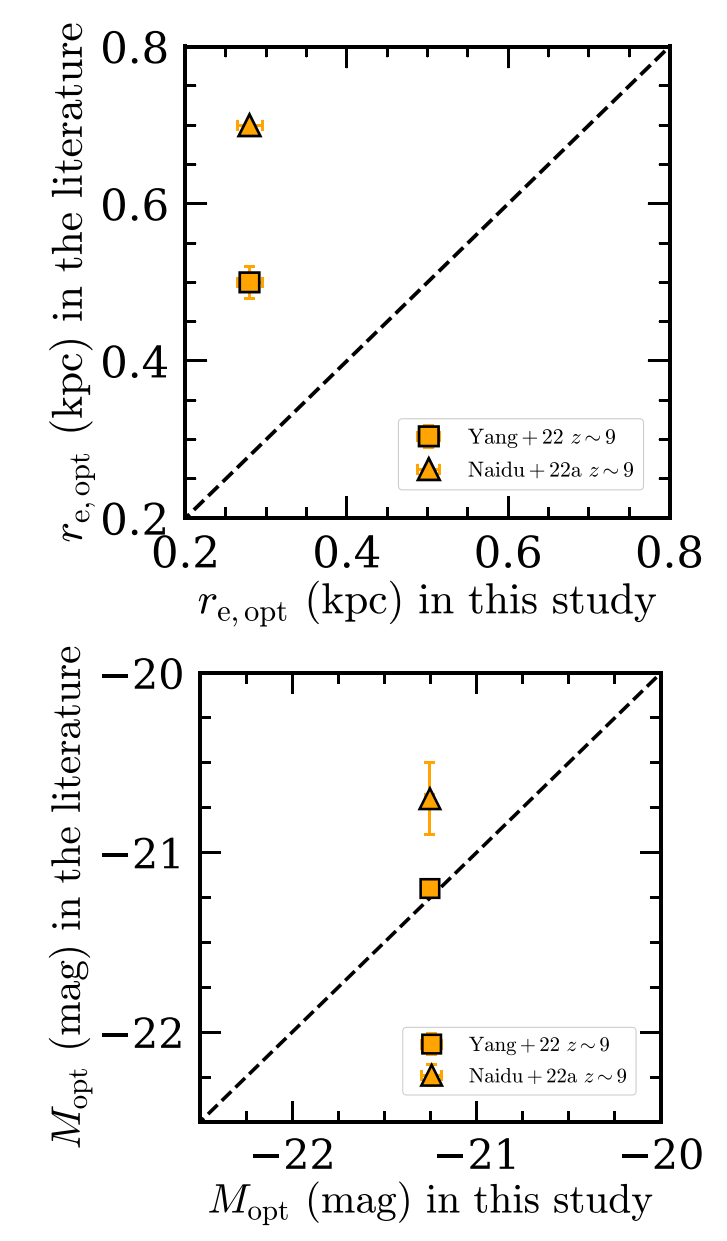
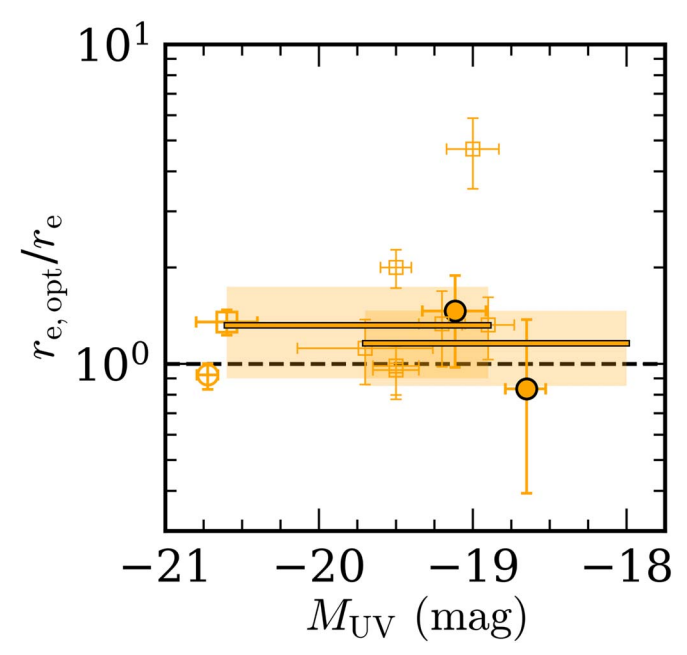


Figure 14. Same as Figure 11, but for the rest-frame optical.

our results for GL-z9-1 and CR2-z12-1 for the brighter bin  $(L/L_{z=3}^* = 0.3-1)$ , and CR2-z12-2, CR2-z12-3, z9-stack-1, and z12-stack-1 for the fainter bin  $(L/L_{z=3}^* = 0.12-0.3)$  as well as the previous HST results. We do not use the result for GL-z12-1 because it is exceptionally compact and may be affected by a possible faint active galactic nucleus (AGN) contribution as discussed in Section 5. The  $z \sim 16$  galaxy candidate is also not used, because it is relatively luminous  $(L/L_{z=3}^* \simeq 2)$ . As in Shibuya et al. (2015), for the uncertainties of the data points of Shibuya et al. (2015), we use the 68th percentiles of the individual size distributions. For the error bars of our data points, we use the individual size measurement uncertainties because of the limited number of our high-z galaxy candidates whose sizes are measured. The obtained slope value for  $L/L_{z=3}^*=0.3-1$  is  $s=-1.22_{-0.16}^{+0.17}$  and that for the fainter luminosity bin of  $L/L_{z=3}^*=0.12-0.3$  is  $s=-1.17_{-0.16}^{+0.16}$ , which are consistent with the previous results for z = 0-8 galaxies, as



**Figure 15.** Ratio of size in the rest-frame optical to that in the rest-frame UV as a function of  $M_{\rm UV}$ . The large open circle denotes our results for GL-z9-1 and the large filled circles correspond to our results for stacked  $z\sim 9$  galaxy candidates with  $L/L_{z=3}^*=0.12-0.3$  and 0.048-0.12. The orange solid line and the orange shading in the faint magnitude range  $(-19.7 \lesssim M_{\rm UV} \lesssim -18.0$  mag) are the average size ratio of these two stacked objects and their uncertainty, respectively. The open squares are the previous results for  $z\sim 7-9$  galaxy candidates with size measurements in F150W and F444W (Yang et al. 2022). The large open square represents their results for GL-z9-1. The orange solid line in the brighter magnitude range  $(-20.6 \lesssim M_{\rm UV} \lesssim -18.9$  mag) is the median size ratio presented in Yang et al. (2022). The black-dashed line denotes the case where the size ratio is unity.

expected from the good agreement of the data points with the extrapolation of the previously obtained size evolution. These fittings should be improved by obtaining size measurements for a larger sample of high-z galaxies through upcoming deep JWST observations.

# 4.5. Star Formation Rate Surface Density

We compare the star formation rate (SFR) surface densities,  $\Sigma_{\rm SFR}$ , of our high-z galaxy candidates with previous results for lower-z galaxies. The SFRs are calculated by using Equation (1) in Kennicutt (1998),

SFR = 
$$1.4 \times 10^{-28} \alpha_{SC} L_{\nu}$$
, (12)

where  $L_{\nu}$  is the rest UV luminosity density in units of erg s<sup>-1</sup> Hz<sup>-1</sup>. We multiply by  $\alpha_{\rm SC} = 0.63$  (Madau & Dickinson 2014) to convert from the Salpeter initial mass function (IMF; Salpeter 1955) to the Chabrier IMF (Chabrier 2003). We then calculate the SFR surface density  $\Sigma_{\rm SFR}$  in units of  $M_{\odot}$  yr<sup>-1</sup> kpc<sup>-2</sup> as the average SFR in a circular region whose half-light radius is  $r_{\rm e}$ ,

$$\Sigma_{\rm SFR} = \frac{\rm SFR}{2\pi r_{\rm e}^2}.\tag{13}$$

The multiplicative factor 1/2 is applied because the SFR is estimated from the total luminosity while the area is calculated with the half-light radius (e.g., Hathi et al. 2008; Tacconi et al. 2013; Decarli et al. 2016).

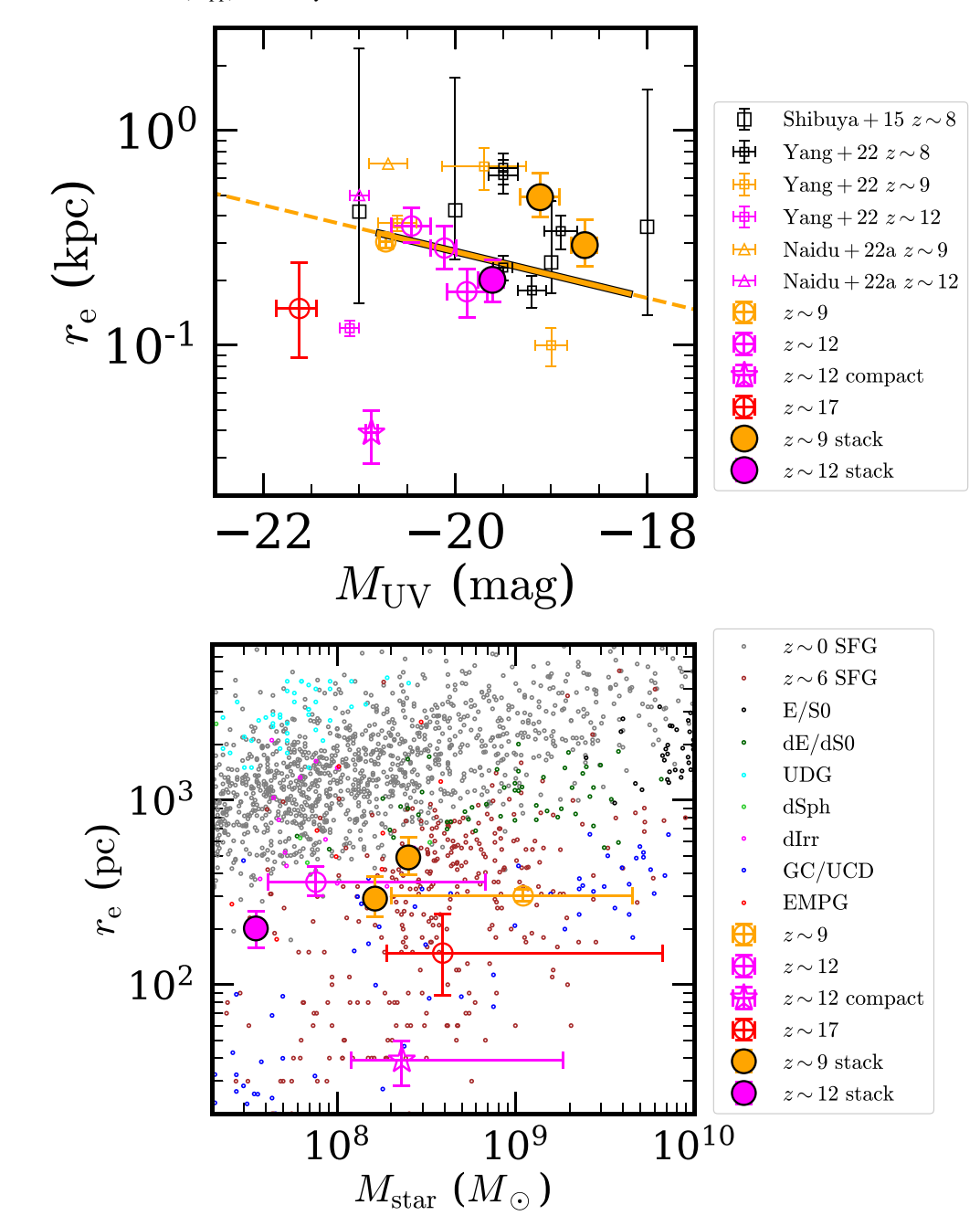


Figure 16. Top: size—luminosity relation for  $z\sim9-16$  galaxy candidates. The orange, magenta, and red large open circles represent bright objects in our  $z\sim9$ ,  $z\sim12$ , and  $z\sim16$  galaxy candidate samples, respectively. The magenta open star denotes the very compact galaxy candidate, GL-z12-1. The orange (magenta) filled circles correspond to the stacked objects of our faint  $z\sim9$  ( $z\sim12$ ) galaxy candidates. The orange solid line denotes the best-fit size—luminosity relation for our  $z\sim9$  galaxy candidates, and the orange dashed line its extrapolation. The small orange and magenta symbols (open squares and triangles) denote previous JWST results for  $z\sim9$  and  $z\sim12$  galaxy candidates, respectively (Yang et al. 2022; Naidu et al. 2022a). The black large open squares denote previous results for  $z\sim8$  galaxy candidates and their large error bars denote the 16th and 84th percentiles of the individual size distribution (Shibuya et al. 2015). The black small open squares represent previous JWST results for galaxy candidates at z<8.5 in Yang et al. (2022). Bottom: size as a function of stellar mass for  $z\sim9-16$  galaxy candidates. The large orange, magenta, and red symbols are the same as those in the top panel. The stellar masses of our stacked objects are calculated by using the stellar mass-to-luminosity ratios for the bright candidates. The other small symbols denote data compiled by Isobe et al. (2021); the gray and brown dots represent SFGs at  $z\sim0$  and  $z\sim6$ , respectively (Shibuya et al. 2015; Kikuchihara et al. 2020); the black dots represent local ellipticals (E/S0; Norris et al. 2014); the dark green dots represent local dwarf spheroidals (dSph; McConnachie 2012); the magenta dots represent local dwarf irregulars (dIrr; McConnachie 2012); the blue dots represent globular clusters and local ultracompact dwarfs (GC/UCD; Norris et al. 2014); and the red dots represent local extremely metal-poor galaxies (EMPGs; Isobe et al. 2021).

In Figure 18, we plot the  $\Sigma_{\rm SFR}$  values as a function of stellar mass for our high-z galaxy candidates and SFGs at lower redshifts. At lower redshifts of z=0–8, the average  $\Sigma_{\rm SFR}$  values increase with redshift at a fixed stellar mass, as reported in Section 5.3 of Shibuya et al. (2015). Our study extends it

toward higher redshifts. At fixed stellar masses of  $\sim 10^{8-9} M_{\odot}$ , we find that our high-z galaxy candidates have consistent or higher  $\Sigma_{\rm SFR}$  values compared to  $z \sim 6-8$  SFGs. In particular, the very compact GL-z12-1 has an exceptionally high  $\Sigma_{\rm SFR}$ , about  $900~M_{\odot}~{\rm yr}^{-1}~{\rm kpc}^{-2}$ .

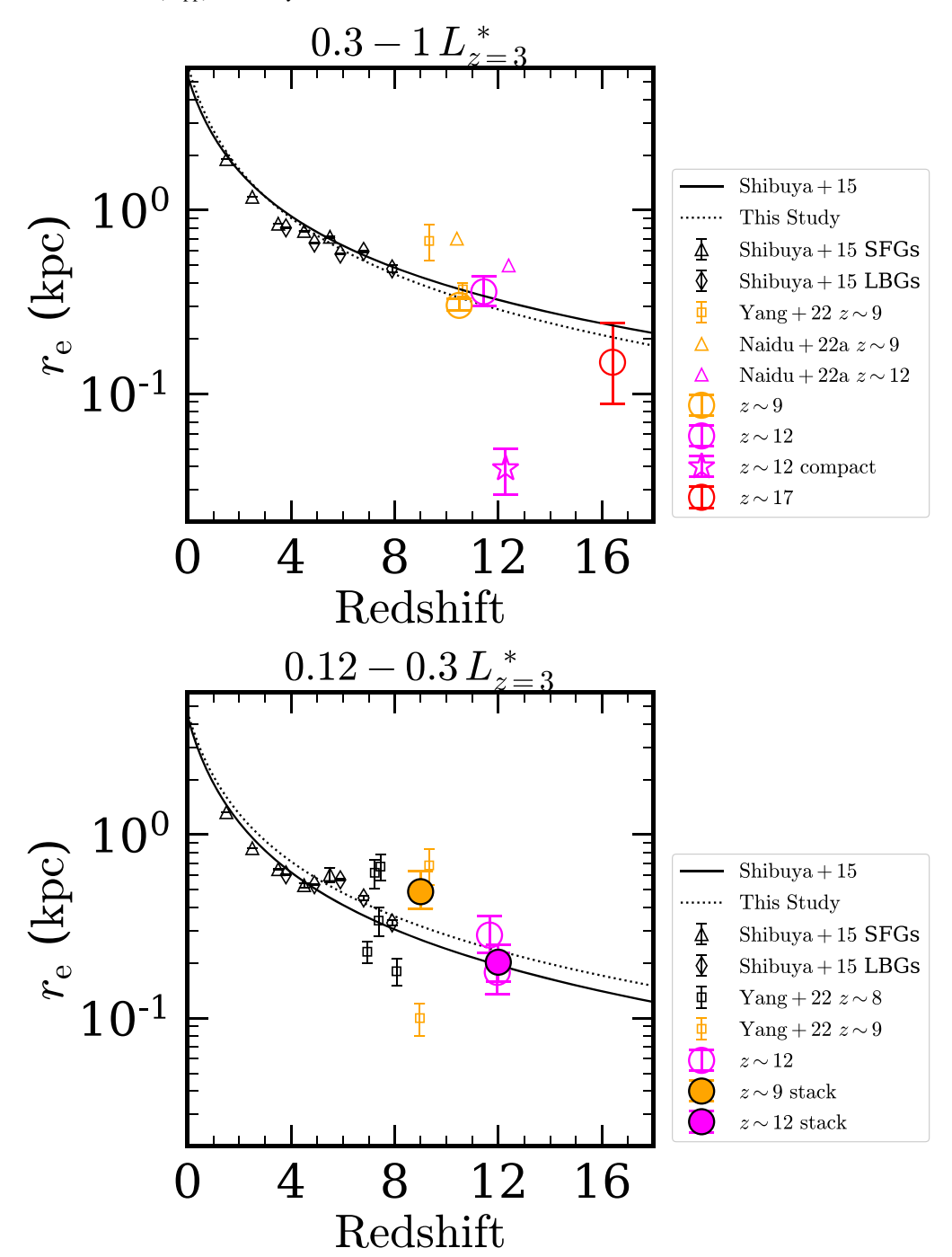


Figure 17. Evolution of the half-light radius of SFGs with UV luminosities of (0.3-1)  $L_{z=3}^*$  (top) and (0.12-0.3)  $L_{z=3}^*$  (bottom). The orange, magenta, and red large open circles show bright objects in our  $z \sim 9$ ,  $z \sim 12$ , and  $z \sim 16$  galaxy candidate samples, respectively. The magenta open star denotes the very compact galaxy candidate, GL-z12-1. The orange (magenta) filled circle denotes the stacked object of our faint  $z \sim 9$  ( $z \sim 12$ ) galaxy candidates. The small orange and magenta symbols (open squares and triangles) denote previous JWST results for  $z \sim 9$  and  $z \sim 12$  galaxy candidates, respectively (Naidu et al. 2022a; Yang et al. 2022). The black small open squares denote previous JWST results for galaxy candidates at z < 8.5 in Yang et al. (2022). The black open triangles and diamonds denote previous results for lower- $z \sim 9$  solutions of the best-fit functions of  $z \sim 9$  obtained in Shibuya et al. (2015) and in this study, respectively.

### 5. Discussion

# 5.1. Very Compact Star Formation at $z \sim 12$

As presented in Section 4, the size of GL-z12-1 is very compact compared to the other candidates and those expected from the size evolution based on the previous HST studies. There are two possible physical origins of such galaxies with very compact morphologies.

One possible physical origin is very compact star formation. Qualitatively, very compact star formation can happen at high redshifts because collapsed haloes are more compact and dense at higher redshifts. Recent 3D radiation hydrodynamic simulations of star cluster formation have suggested that when an initial gas surface density is sufficiently high, most of the gas in molecular gas clouds can be converted into stars with very high star formation efficiencies thanks to the inefficiency of star

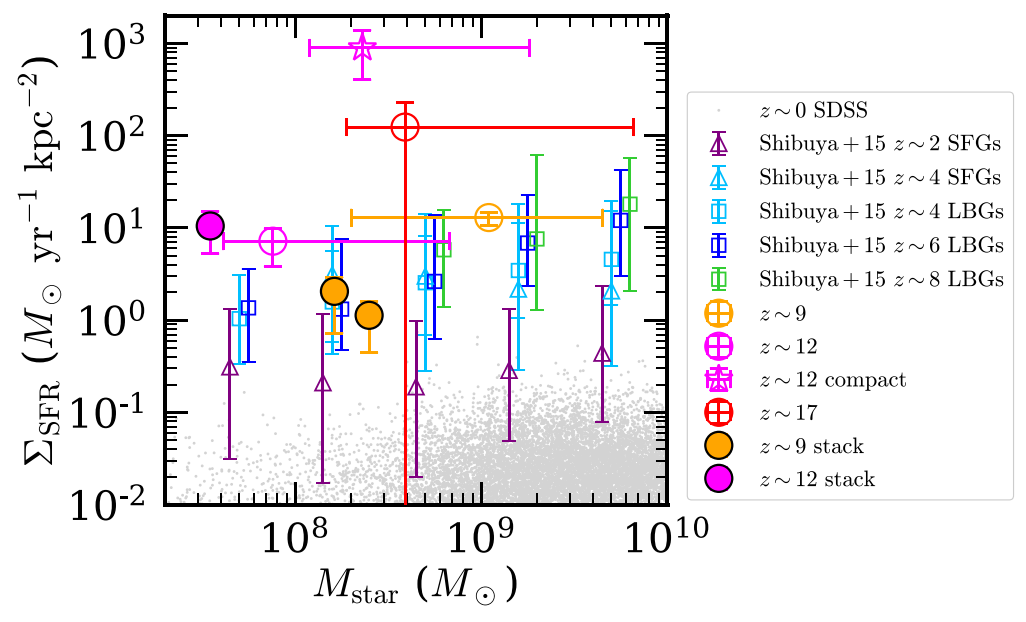
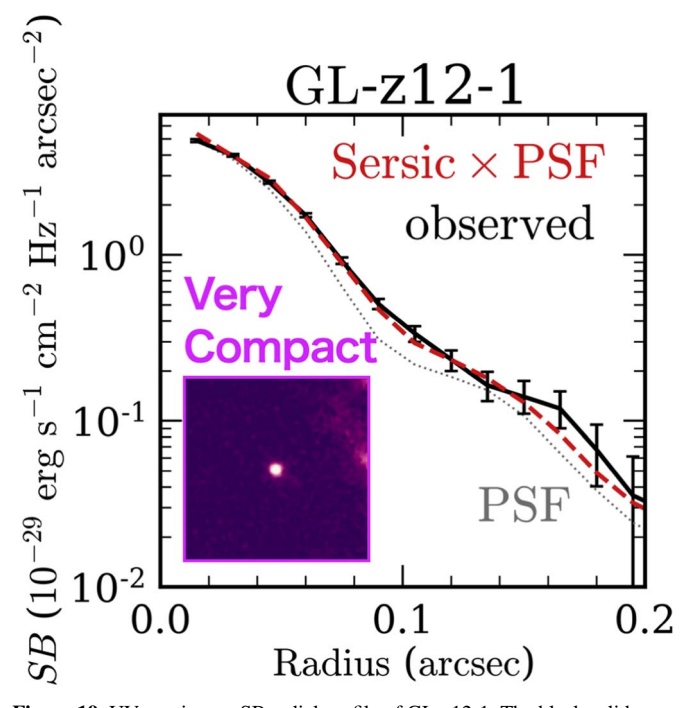
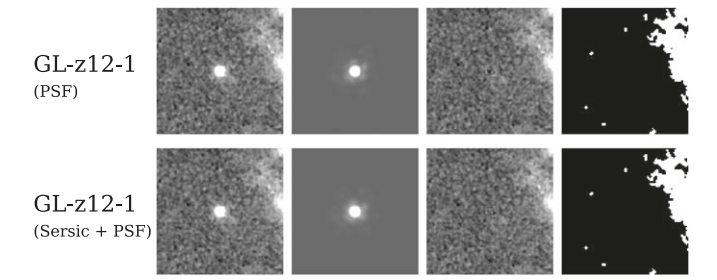


Figure 18. SFR surface density  $\Sigma_{\rm SFR}$  vs. stellar mass  $M_{\rm star}$ . The orange, magenta, and red open circles show bright objects in our  $z\sim9$ ,  $z\sim12$ , and  $z\sim16$  galaxy candidate samples, respectively. The orange (magenta) filled circle denotes the stacked object of our faint  $z\sim9$  ( $z\sim12$ ) galaxy candidates. The open triangles indicate SFGs at  $z\sim2$  (purple) and  $z\sim4$  (cyan). The open squares denote LBGs at  $z\sim4$  (cyan),  $z\sim6$  (blue), and  $z\sim8$  (green). The gray dots denote Sloan Digital Sky Survey (SDSS) galaxies compiled by Shibuya et al. (2015); the  $\Sigma_{\rm SFR}$  values are calculated based on the catalog of Lackner & Gunn (2012), and the stellar masses for the SDSS galaxies are taken from Kauffmann et al. (2003), Brinchmann et al. (2004), and Salim et al. (2007).



**Figure 19.** UV continuum SB radial profile of GL-z12-1. The black solid curve corresponds to the observed SB profile in F200W. The  $1\sigma$  uncertainties are calculated based on the 68th percentiles of radial profiles obtained at randomly selected positions in the F200W image. The red dashed curve denotes the best-fit Sérsic profile convolved with the PSF. The gray dotted curve represents the PSF profile whose peak is normalized by the peak of the observed profile to clarify the profile difference. The inset panel is the 1."5  $\times$  1."5 cutout of the original image.

formation suppression by ionizing radiation in high-density regions (Fukushima & Yajima 2021; see also, Kim et al. 2018; Fukushima et al. 2020), and such objects may be observed as very compact SFGs. In fact, the  $\Sigma_{SFR}$  value of GL-z12-1 is very high, about  $900~M_{\odot}~\rm{yr}^{-1}~\rm{kpc}^{-2}$ . If it hosts very compact star formation, it may



**Figure 20.** Further SB profile fitting results for GL-z12-1. The top panels present the results with a zero-size PSF for GL-z12-1. The bottom panels show the results for GL-z12-1 with a superposition of a zero-size PSF for the possible AGN contribution and a Sérsic profile for the host galaxy.

correspond to actively forming young massive star clusters in a compact region some of which would evolve into present-day globular clusters (e.g., Kruijssen 2014). For lower mass galaxies, recent theoretical studies on globular cluster formation based on cosmological simulations have been reported in Sameie et al. (2023). It would be interesting to compare with these theoretical results if high-z galaxies with similar low masses are found in future JWST observations such as for galaxy cluster regions where gravitational lensing effects are strong.

The other possible physical origin is AGNs. If the AGN contribution is dominant, their SB profiles are expected to be mostly explained with the PSF profiles. However, as shown in Figure 19, we find that its radial profile is clearly more extended than the PSF profile. This can also be confirmed by the SB profile fitting. In the top panels of Figure 20, we present the results of the profile fitting with a PSF for GL-z12-1. In this case, the free parameters are the centroid coordinates and the total magnitude. The residual image clearly shows a systematically negative region around the center, indicating that the PSF fitting result is not as good as the Sérsic profile fitting

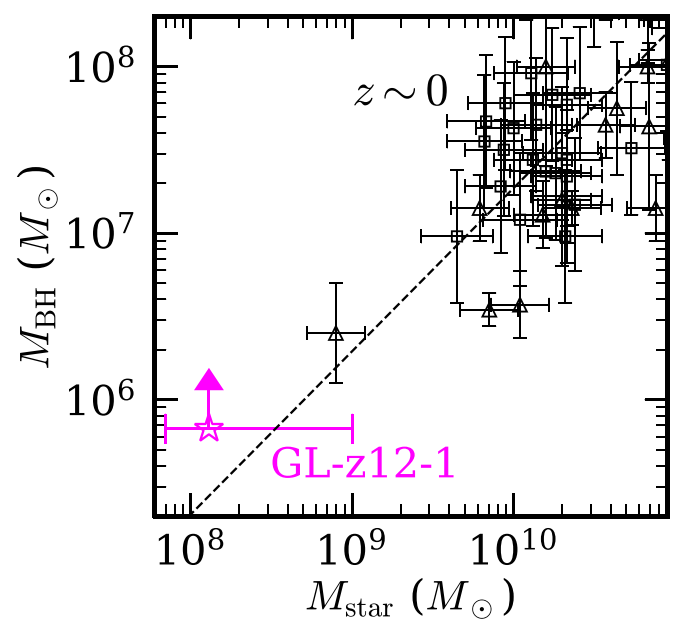


**Figure 21.** Central black hole mass vs. stellar mass. The magenta open star denotes GL-z12-1, whose black hole mass lower limit is calculated from the UV luminosity in the case of the Eddington limit. The black open triangles and squares denote the local galaxies in Häring & Rix (2004) and Bennert et al. (2011), respectively, compiled by Ding et al. (2020). The dashed line denotes the best-fit local relation,  $\log(M_{\rm BH}/10^7M_{\odot})=0.27~+~0.98\log(M_{\rm star}/10^{10}M_{\odot})$ , presented in Figure 7 of Ding et al. (2020).

result. These results suggest that the AGN contribution is not dominant to its SB profile.

The possibility that GL-z12-1 hosts a faint AGN cannot be ruled out based on the comparison only with the PSF. To examine it, we perform the SB profile fitting with a composite of two components: a PSF profile for the possible faint AGN component and a Sérsic profile for the host galaxy component. The bottom panel of Figure 20 presents the results of the twocomponent profile fitting. Because there are almost no systematically negative or positive regions around the center of the residual image, the SB profile of GL-z12-1 is characterized well by the two components. The obtained total magnitudes in the two-component fitting are  $M_{\rm UV}=-20.0^{+0.4}_{-0.4}$  mag for the PSF component and  $M_{\rm UV}=-20.2^{+0.3}_{-0.3}$  mag for the Sérsic component. Importantly, even in this two-component fitting, the size of the Sérsic component is still small,  $r_{\rm e} = 48^{+38}_{-15}$  pc, which means that even with a faint AGN, a very compact star-forming component is needed to explain the SB profile of GL-z12-1.

In the discussion above, we consider compact star formation and AGNs as possible physical origins for the very compact size of GL-z12-1. Based on the detailed analyses with its SB profile, we find that, even if GL-z12-1 hosts a faint AGN, it still needs a very compact Sérsic component, suggesting that we detect extremely compact star formation at  $z \sim 12$  for the first time thanks to the great sensitivity and resolution of JWST.

## 5.2. A Possible Faint AGN at $z \sim 12$ ?

Although the two-component fitting result for GL-z12-1 does not strongly suggest the existence of a faint AGN in it, we compare this possible faint AGN with the Magorrian relation (e.g., Kormendy & Ho 2013). The bolometric luminosity of the PSF component of GL-z12-1 converted from the UV

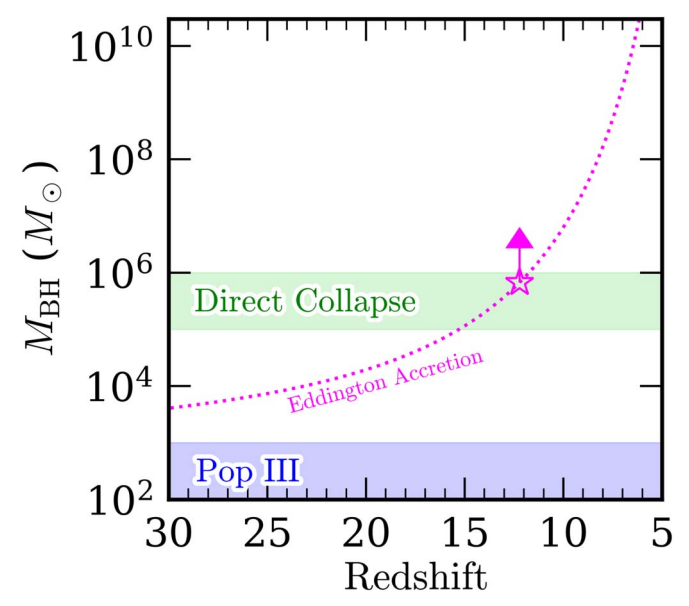


Figure 22. Central black hole mass as a function of redshift. The magenta open star denotes GL-z12-1, whose black hole mass lower limit is calculated from the UV luminosity in the case of the Eddington limit. The magenta-dotted curve corresponds to the expected growth history of the central black hole in GL-z12-1 in the case of the Eddington limit. The green and blue shaded regions denote the seed mass range of direct collapse black holes ( $M_{\rm seed} \sim 10^{5-6} M_{\odot}$ ; Latif & Ferrara 2016) and that of Population III remnant black holes ( $M_{\rm seed} \lesssim 10^3 M_{\odot}$ ; Hirano et al. 2014), respectively.

luminosity is  $L_{\rm bol} \simeq 8.7 \times 10^{43}$  erg s<sup>-1</sup>. In the case of the Eddington limit,  $L_{\rm bol} = L_{\rm Edd} = 1.3 \times 10^{38} M_{\rm BH}$  (e.g., Rybicki & Lightman 1979), where  $L_{\rm Edd}$  is the Eddington luminosity and  $M_{\rm BH}$  is the central black hole mass, we obtain  $M_{\rm BH} \simeq$  $6.7 \times 10^5 M_{\odot}$ , corresponding to the lower limit of the central black hole mass in GL-z12-1. In Harikane et al. (2023), the stellar mass of GL-z12-1 is estimated to be  $\simeq 2.3 \times 10^8 M_{\odot}$ based on the SED fitting (see their Section 3.3 and Table 10). Because this stellar mass is derived from the SED with the total luminosities, by scaling the stellar mass by the UV luminosity based on the two-component fitting result, we obtain the stellar mass of the host galaxy,  $M_{\rm star} \simeq 1.3 \times 10^8 M_{\odot}$ . Figure 21 compares the stellar and central black hole masses of GL-z12-1 with those of local objects in the literature compiled by Ding et al. (2020) (see also, Häring & Rix 2004; Bennert et al. 2011). The results of GL-z12-1 are consistent with the extrapolation of the relation between  $M_{\rm BH}$  and  $M_{\rm star}$  in the nearby universe to the low-mass regime.

It is also interesting to check whether such a massive black hole can be formed by  $z \sim 12$ . The black hole mass  $M_{\rm BH}$  increases exponentially with time t from the seed black hole with a mass of  $M_{\rm seed}$  at a fixed Eddington ratio (e.g., Bañados et al. 2018; Onoue et al. 2019),

$$M_{\rm BH} = M_{\rm seed} \exp\left(\frac{t}{\tau}\right),$$
 (14)

where  $\tau$  is the *e*-folding timescale,

$$\tau = 0.45 \left(\frac{\eta}{1-\eta}\right) \left(\frac{L_{\text{bol}}}{L_{\text{Edd}}}\right)^{-1} \text{Gyr.}$$
 (15)

We adopt the radiation efficiency of  $\eta = 0.1$ , which corresponds to a standard thin accretion disk (Shakura & Sunyaev 1976). In this case,  $\tau = 50$  Myr. The estimated growth

history of the black hole with the estimated mass at  $z \sim 12$  at the Eddington limit is plotted in Figure 22. If this black hole grows at the Eddington limit toward lower redshifts, the expected black hole mass at  $z \sim 6-7$  is  $\sim 10^{9-10} M_{\odot}$ , which is comparable to those of central supermassive black holes in  $z \sim 6-7$  QSOs found in the previous work (e.g., Wu et al. 2015; Bañados et al. 2018; Onoue et al. 2019; Shen et al. 2019; Yang et al. 2020, 2021; Wang et al. 2021). For higher redshifts, even if the mass of this black hole increases at the Eddington limit, it does not fall within the mass range of seed black holes formed from Population III remnants,  $M_{\rm seed} \lesssim 10^3 M_{\odot}$  (e.g., Hirano et al. 2014), at z < 30, when the first stars and galaxies are thought to have formed (e.g., Bromm & Yoshida 2011). If the black hole mass of GL-z12-1 at  $z \sim 12$  is even larger and/or the black hole growth rate is smaller than the Eddington limit, it is more difficult to explain its seed black hole with Population III remnants. This may suggest the possibility that the central black hole of GL-z12-1 is formed by the direct collapse of primordial gas clouds, which can result in more massive seed black holes with  $\sim 10^{5-6} M_{\odot}$  (e.g., Latif & Ferrara 2016).

At this moment, we cannot distinguish whether GL-z12-1 hosts very compact star formation with or without a faint AGN based on the currently available data. Although the number density of faint AGNs at  $M_{\rm UV} \simeq -20.0$  mag at  $z \sim 12$  is expected to be very low compared to that of galaxies (e.g., Figure 4 of Finkelstein & Bagley 2022), implying that the probability of finding a faint AGN at this high redshift is not high, deep follow-up observations for exceptionally compact high-z candidates may be helpful to examine the existence of a very high-z intermediate-mass black hole at an early phase of black hole formation.

# 5.3. Comparison with Cosmological Zoom-in Simulation Results

As described above, we have found that one of our  $z \sim 12$  galaxy candidates, GL-z12-1, has a very compact size of 40 pc in the rest-frame UV continuum. We have also found that the average size of  $z \sim 9$ -16 galaxy candidates is around 200–500 pc. Here we compare these observational results with two theoretical study results for galaxies with comparable stellar masses at similar redshifts.

First, we compare our results with those in Yajima et al. (2022b), who performed cosmological hydrodynamics zoom-in simulations to study galaxy formation and evolution in a large comoving volume of  $(714\,\mathrm{Mpc})^3$  for the project named FOREVER22 (see also, Yajima et al. 2022a). Based on their results of the most high-resolution run with a mass resolution of  $\sim 8 \times 10^3 M_\odot$  (first run), we focus on a single galaxy with stellar masses of about  $10^{8-9} M_\odot$  at  $z \sim 9$ –12 that are comparable to those of our galaxy candidates. We extract its 2D projected stellar mass density distributions from z=17 to z=9.5 for comparison.

The evolution of its half-light radius and stellar mass is compared with our observational results in the top panel of Figure 23. The stellar mass of the simulated galaxy increases with decreasing redshift, while the size becomes smaller and larger. Interestingly, at z=9.5, the simulated galaxy has a comparable stellar mass and a similar or smaller size compared to GL-z12-1. In the top panel of Figure 23, we also present the stellar mass density distribution for the simulated galaxy at

each redshift as an inset panel near each data point. At z=9.5, the simulated galaxy is relatively isolated with intense matter inflow from the surroundings along the filaments involving minor mergers. Our finding of the very compact nature of GLz12-1 would be the first observational evidence of very compact SFGs at high redshifts that naturally form in theoretical studies.

These physical processes may be similar to those taking place as the compaction, which is discussed for the formation of  $z \sim 2$ –4 compact galaxies, so-called blue nuggets (Zolotov et al. 2015; Tacchella et al. 2016). Note that the size of GL-z12-1 is much smaller than those of the simulated galaxies with comparable stellar masses at z=2 in Tacchella et al. (2016) (see their Table 1). Such very compact star formation can happen at high redshifts because collapsed haloes at higher redshifts are more compact and dense.

At z=11–13, the simulated galaxy by Yajima et al. (2022b) has similar stellar masses and sizes to those of our faint stacked objects. As shown in the inset panels in the top panel of Figure 23, at these redshifts, major mergers and/or tidal interactions with surrounding objects are taking place, which would imply that most of our high-z galaxy candidates are experiencing a major merger and/or interaction events. The major merger rate increases with increasing redshift, and galaxies experience  $\sim$ 1–2 major mergers on average by z=10 based on the Illustris simulation results (Rodriguez-Gomez et al. 2015). Because the age of the universe is only  $\sim$ 500 Myr at z=10, which corresponds to several times the dynamical time at z=10 ( $\sim$ 100 Myr), morphologies of galaxies at  $z\gtrsim$ 10 are expected to be strongly affected by major mergers for most of the time since their formation.

Next, we also compare our observational results with the theoretical results of another zoom-in simulation suite that is focused on high-redshift galaxy formation called the Renaissance Simulations (Xu et al. 2016; Barrow et al. 2017). We extract five simulated galaxies at z = 10-15 with similar stellar masses to our galaxy candidates,  $M_{\rm star} \sim 10^{7-8} M_{\odot}$ , and calculate their half-light radii for comparison as presented in the bottom panel of Figure 23. We calculate their SBs and halflight radii using the stellar spectra in the rest-frame UV at 1500 Å. These simulated galaxies have similar stellar masses and sizes to those of our  $z \sim 12$  stacked object. As shown in the inset panels in the bottom panel of Figure 23, all of these simulated galaxies either show an elongated morphology or are accompanied by diffuse structures, indicating evidence of mergers and/or interactions with nearby objects. This may suggest that most of our high-z galaxy candidates are undergoing mergers and/or interactions, in a similar way to the results of Yajima et al. (2022b).

The high sensitivity and resolution of JWST have made it possible to investigate the morphological properties of galaxies at such high redshifts that can be compared with cosmological hydrodynamics zoom-in simulation results. However, at this early stage of JWST explorations, the number of high-z galaxy candidates is limited. Deeper JWST images and/or larger highz galaxy samples would be needed for a more robust discussion of their morphological properties.

# 6. Summary

In this study, we have presented the SB profile fitting results for the  $z\sim9$ –16 galaxy candidates, which are securely selected with the conservative photo-z determination criteria  $\Delta\chi^2>9$  as

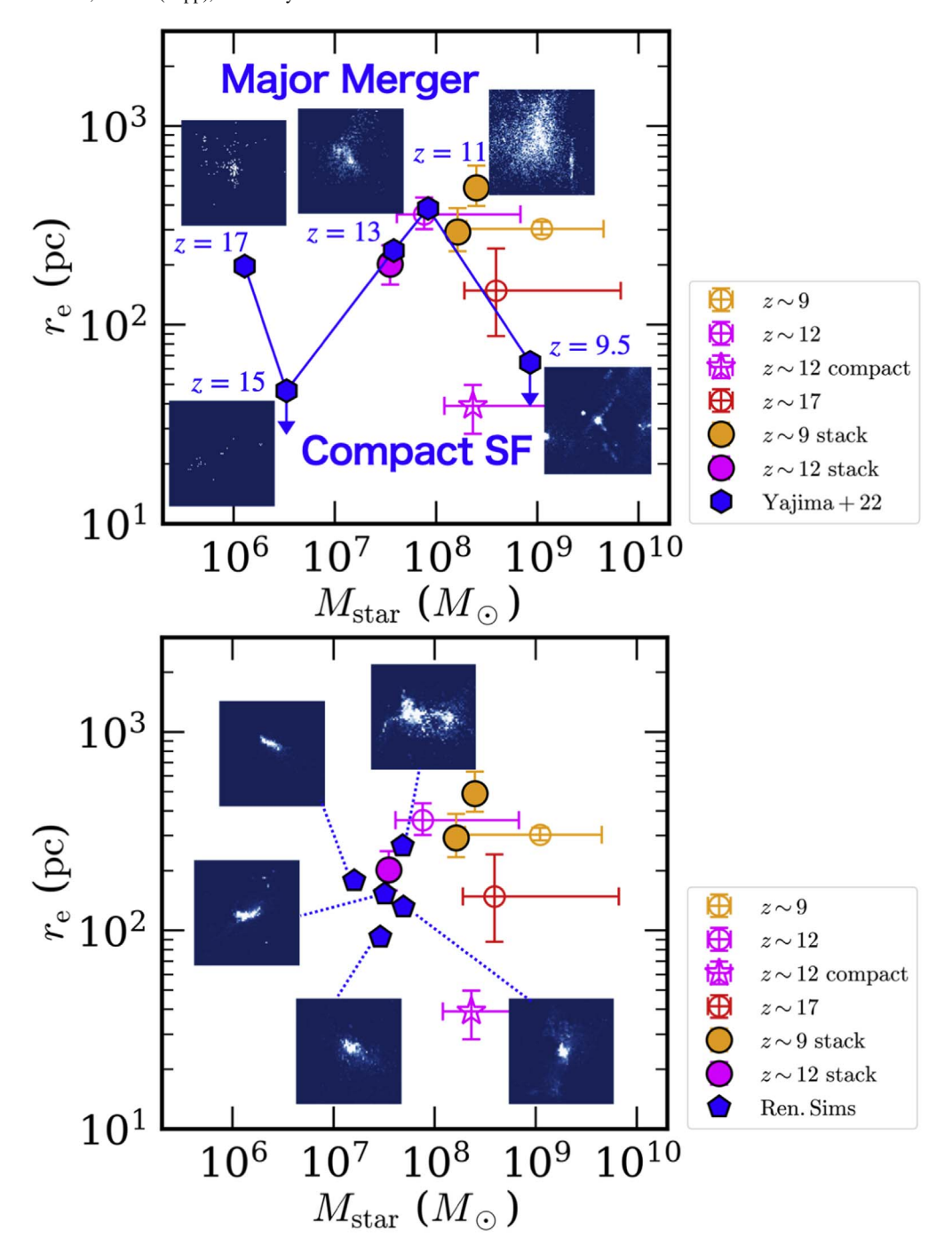


Figure 23. Comparison with the results of theoretical studies on the half-light radius vs. stellar mass plane. Top: the blue hexagons represent the evolution of an SFG from z = 17–9.5 with similar stellar masses and redshifts to our candidates in a cosmological hydrodynamics zoom-in simulation (Yajima et al. 2022b). Each inner image is a 1.75 × 1.75 snapshot of the 2D projected stellar mass distribution at each redshift. The other symbols are the same as the bottom panel of Figure 16. Bottom: The blue pentagons denote SFGs at z = 10–15 with similar stellar masses to our candidates extracted from the Renaissance Simulations (Xu et al. 2016; Barrow et al. 2017). Each inner image corresponds to a  $\simeq 1.77$  snapshot of the SB of each simulated galaxy. The other symbols are the same as those in the bottom panel of Figure 16.

well as the conventional color criteria with the deep JWST NIRCam images taken by the four ERS and ERO programs, i.e., ERS GLASS, ERS CEERS, ERO SMACS J0723, and ERO Stephan's Quintet. One of these candidates has been spectroscopically identified at z=11.44 by recent JWST/NIRSpec spectroscopy. In the same manner as the previous work, we correct for the systematic effects that galaxy sizes and luminosities are systematically underestimated for faint objects by performing MC simulations. Our main results are as follows:

- 1. Our SB profile fitting results indicate that most of our  $z \sim 9{\text -}16$  galaxy candidates have sizes (half-light radii) of  $r_{\rm e} \sim 200{\text -}500$  pc, which is comparable to previous HST results for high-z galaxies with similar UV luminosities. We have also found that one of our  $z \sim 12$  galaxy candidates, GL-z12-1, shows an exceptionally compact size of  $39 \pm 11$  pc.
- 2. The sizes of our  $z \sim 9$  galaxy candidates in the rest-frame optical are comparable to those in the rest-frame UV. The average size ratio between the rest UV and optical for our

- faint stacked objects is consistent with unity, suggesting that the distributions of massive stars and less massive ones in faint galaxies are similar, probably because of recent star formation activities in low-mass galaxies.
- 3. The UV size-luminosity relation at  $z \sim 9-12$  does not change significantly from the previous results at  $z \sim 8$ . The stellar masses and sizes of our bright galaxy candidates at  $z \sim 9-16$  are comparable to previously reported values for  $z \sim 6$  SFGs and local UCDs.
- 4. The sizes of our  $z \sim 10$ –16 galaxy candidates with  $L/L_{z=3}^* = 0.12$ –0.3 and  $L/L_{z=3}^* = 0.3$ –1 are broadly consistent with the extrapolation of the galaxy size evolution based on the previous HST results at  $z \sim 0$ –10.
- 5. The SFR surface densities of our bright high-z galaxy candidates are consistent with or higher than those of  $z\sim 6-8$  SFGs at fixed stellar masses. In particular, GLz12-1 shows an exceptionally high  $\Sigma_{\rm SFR}$  value because of its very compact nature.
- 6. The SB profile of the very compact galaxy candidate GLz12-1 requires a compact Sérsic component even when we consider the possibility of having a faint AGN. Our results indicate that GL-z12-1 hosts very compact star formation with or without a faint AGN.
- 7. If GL-z12-1 has a faint AGN, its central black hole mass and stellar mass expected from its luminosity and SED are consistent with the extrapolation of the local  $M_{\rm BH}$ – $M_{\rm star}$  relation. It is difficult to explain the seed black hole mass of GL-z12-1 with Population III remnants, which may suggest the possibility of the direct collapse scenario.
- 8. Recent cosmological simulations for a galaxy with comparable stellar masses at  $z \sim 9-12$  indicate that it can host very compact star formation that is consistent with GL-z12-1, and can also have star formation whose sizes are comparable to those of our stacked objects, depending on its evolution phase. The comparisons with the simulation results suggest that very compact star formation as observed in GL-z12-1 corresponds to a relatively isolated phase with intense accretion of material, while star formation with 200–500 pc sizes corresponds to a phase of major merger and/or interaction with the surrounding objects.

# Acknowledgments

We thank Marcio B. Meléndez for giving us helpful advice on how to use WebbPSF. This work is based on observations made with the NASA/ESA/CSA JWST. The data were obtained from the Mikulski Archive for Space Telescopes at the Space Telescope Science Institute, which is operated by the Association of Universities for Research in Astronomy, Inc., under NASA contract NAS 5-03127 for JWST. These observations are associated with programs 2732, 2736, 1324, and 1345. We acknowledge the ERO, GLASS, and CEERS teams led by Klaus M. Pontoppidan, Tommaso Treu, and

Steven L. Finkelstein, respectively, for developing their observing programs with a zero-exclusive-access period. This work was partially performed using the computer facilities of the Institute for Cosmic Ray Research, The University of Tokyo. This work was supported by the World Premier International Research Center Initiative (WPI Initiative), MEXT, Japan, as well as KAKENHI grant Nos. 15K17602, 15H02064, 17H01110, 17H01114, 19K14752, 20H00180, 21H04467, and 22K03670 through the Japan Society for the Promotion of Science (JSPS). J.H.W. is supported by NSF grants OAC-1835213 and AST-2108020 and NASA grants 80NSSC20K0520 and 80NSSC21K1053. This work was partially supported by the joint research program of the Institute for Cosmic Ray Research (ICRR), University of Tokyo.

*Software:* GALFIT (Peng et al. 2002, 2010), SExtractor (Bertin & Arnouts 1996), IRAF (Tody 1986, 1993), <sup>15</sup> SAO-Image DS9 (Joye & Mandel 2003), NumPy (Harris et al. 2020), Matplotlib (Hunter 2007), SciPy (Virtanen et al. 2020), Astropy (Astropy Collaboration et al. 2013, 2018), <sup>16</sup> Ned Wright's Javascript Cosmology Calculator (Wright 2006). <sup>17</sup>

# Appendix MC Simulation Results for Varying Input Sérsic Index Values

In Section 3, we perform the 2D SB profile fittings for our high-z galaxy candidates at  $z \sim 9{\text -}16$  with a fixed Sérsic index of n=1.5, which is the median value obtained in previous work with HST for SFGs with similar UV luminosities to those of our high-z galaxy candidates (Shibuya et al. 2015). However, the constraints on the Sérsic index of SFGs at high redshifts comparable to our candidates are still limited. There is a possibility that the Sérsic index values of such high-z galaxies have a large scatter, which would result in a non-negligible systematic uncertainty in our measurements. To demonstrate the effect of such uncertainty, we perform MC simulations with the F150W data for the GLASS field, following the same procedure as in Section 3 but with the input Sérsic index randomly chosen between 0.5 and 5.0 as an extreme example.

Figure 24 shows the results of size measurements for our MC-simulated galaxies. The dispersions of the data points are significantly larger compared to Figure 4, as expected from the large scatter of the input Sérsic index values. Similarly, Figure 25 presents the results of total magnitude measurements for our MC-simulated galaxies, indicating that the dispersions of the data points are larger than those in Figure 6 as expected again. These MC simulation results imply that if the Sérsic index of high-z galaxies has a uniform distribution from 0.5-5.0, size and total magnitude measurements obtained with a fixed Sérsic index of n = 1.5 have large dispersions. However, if the distribution of the Sérsic index is not so broad, the dispersions of the measurements are not as large as those obtained in these MC simulations. To address this point, we need to obtain better constraints on the Sérsic index of highz galaxies based on sufficiently high S/N data in the future.

IRAF is distributed by the National Optical Astronomy Observatory, which is operated by the Association of Universities for Research in Astronomy (AURA) under a cooperative agreement with the National Science Foundation.
 http://www.astropy.org

<sup>17</sup> http://www.astro.ucla.edu/~wright/CosmoCalc.html

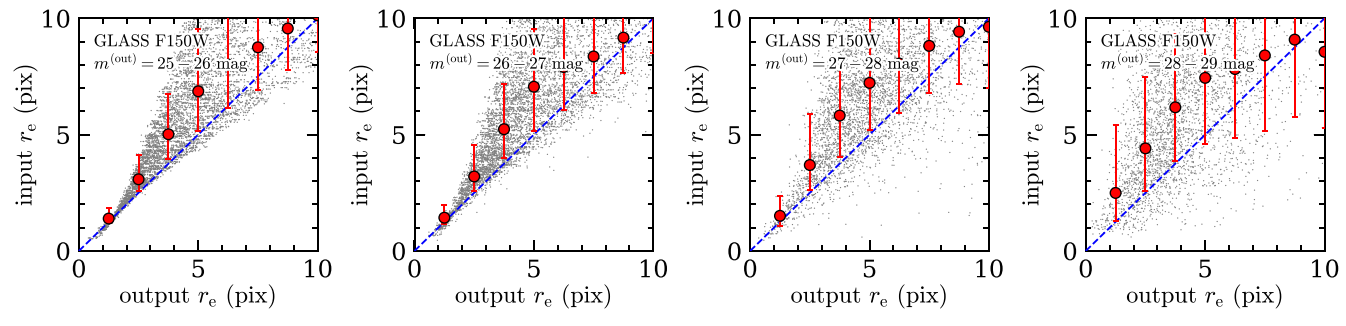


**Figure 24.** Same as Figure 4, except that the input Sérsic index values range from n = 0.5-5.0.

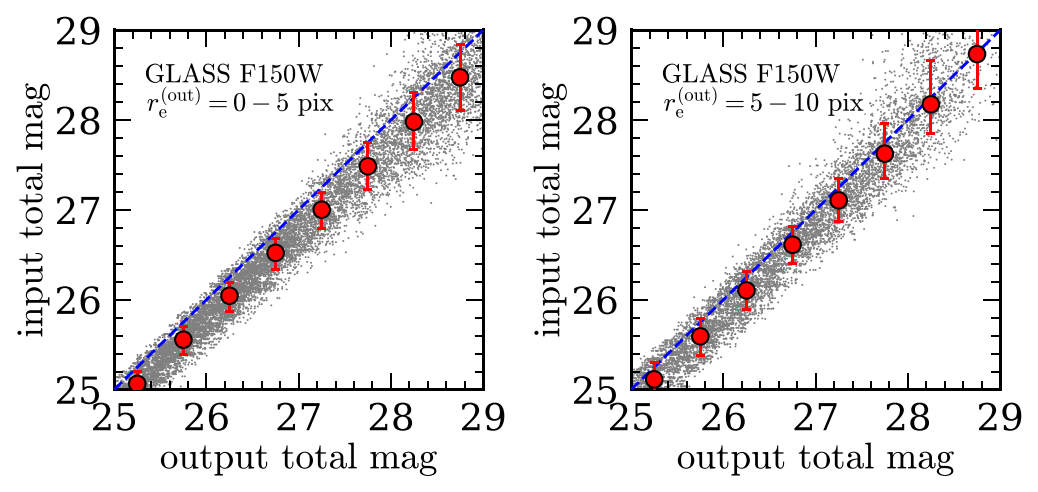


Figure 25. Same as Figure 6, but with the input Sérsic index n randomly chosen between 0.5 and 5.0.

# ORCID iDs

Yoshiaki Ono https://orcid.org/0000-0001-9011-7605 Yuichi Harikane https://orcid.org/0000-0002-6047-430X Masami Ouchi https://orcid.org/0000-0002-1049-6658 Hidenobu Yajima https://orcid.org/0000-0002-1319-3433 Yuki Isobe https://orcid.org/0000-0001-7730-8634 John H. Wise https://orcid.org/0000-0003-1173-8847 Yechi Zhang https://orcid.org/0000-0003-3817-8739 Kimihiko Nakajima https://orcid.org/0000-0003-2965-5070

# References

Adams, N. J., Conselice, C. J., Ferreira, L., et al. 2023, MNRAS, 518, 4755 Allen, R. J., Kacprzak, G. G., Glazebrook, K., et al. 2017, ApJL, 834, L11 Arrabal Haro, P., Dickinson, M., Finkelstein, S. L., et al. 2023, arXiv:2303. 15431 Astropy Collaboration, Price-Whelan, A. M., Sipőcz, B. M., et al. 2018, AJ, Astropy Collaboration, Robitaille, T. P., Tollerud, E. J., et al. 2013, A&A, 558, A33 Atek, H., Shuntov, M., Furtak, L. J., et al. 2023, MNRAS, 519, 1201 Bañados, E., Venemans, B. P., Mazzucchelli, C., et al. 2018, Natur, 553, 473 Barrow, K. S. S., Wise, J. H., Norman, M. L., O'Shea, B. W., & Xu, H. 2017, Bennert, V. N., Auger, M. W., Treu, T., Woo, J.-H., & Malkan, M. A. 2011, ApJ, 726, 59

Bertin, E., & Arnouts, S. 1996, A&AS, 117, 393

Bouwens, R. J., Illingworth, G. D., Blakeslee, J. P., Broadhurst, T. J., & Franx, M. 2004, ApJ, 611, L1

Bouwens, R. J., Illingworth, G. D., Blakeslee, J. P., & Franx, M. 2006, ApJ,

Bouwens, R. J., Illingworth, G. D., Oesch, P. A., et al. 2017, ApJ, 843, 41 Bouwens, R. J., Illingworth, G. D., van Dokkum, P. G., et al. 2021, AJ, 162, 255

927, 81 Bowler, R. A. A., Dunlop, J. S., McLure, R. J., & McLeod, D. J. 2017, MNRAS, 466, 3612 Bridge, J. S., Holwerda, B. W., Stefanon, M., et al. 2019, ApJ, 882, 42 Brinchmann, J., Charlot, S., White, S. D. M., et al. 2004, MNRAS, 351, 1151 Bromm, V., & Yoshida, N. 2011, ARA&A, 49, 373 Bruzual, G., & Charlot, S. 2003, MNRAS, 344, 1000 Castellano, M., Fontana, A., Treu, T., et al. 2022, ApJL, 938, L15 Chabrier, G. 2003, PASP, 115, 763 Conselice, C. J. 2014, ARA&A, 52, 291 Costantin, L., Pérez-González, P. G., Vega-Ferrero, J., et al. 2023, ApJ, 946, 71 Cullen, F., McLure, R. J., McLeod, D. J., et al. 2023, MNRAS, 520, 14 Curtis-Lake, E., McLure, R. J., Dunlop, J. S., et al. 2016, MNRAS, 457, 440 Decarli, R., Walter, F., Aravena, M., et al. 2016, ApJ, 833, 70 Ding, X., Silverman, J., Treu, T., et al. 2020, ApJ, 888, 37 Donnan, C. T., McLeod, D. J., Dunlop, J. S., et al. 2023, MNRAS, 518, 6011 Ferguson, H. C., Dickinson, M., Giavalisco, M., et al. 2004, ApJ, 600, L107 Finkelstein, S. L., & Bagley, M. B. 2022, ApJ, 938, 25 Finkelstein, S. L., Bagley, M. B., Haro, P. A., et al. 2022, ApJL, 940, L55 Fukushima, H., & Yajima, H. 2021, MNRAS, 506, 5512 Fukushima, H., Yajima, H., Sugimura, K., et al. 2020, MNRAS, 497, 3830 Furtak, L. J., Shuntov, M., Atek, H., et al. 2023, MNRAS, 519, 3064 Gardner, J. P., Mather, J. C., Abbott, R., et al. 2023, arXiv:2304.04869 Grazian, A., Castellano, M., Fontana, A., et al. 2012, A&A, 547, A51 Harikane, Y., Ouchi, M., Oguri, M., et al. 2023, ApJS, 265, 5 Häring, N., & Rix, H.-W. 2004, ApJ, 604, L89 Harris, C. R., Millman, K. J., van der Walt, S. J., et al. 2020, Natur, 585, 357 Hashimoto, D., Macias, O., Nishizawa, A. J., et al. 2020, JCAP, 2020, 059 Hathi, N. P., Malhotra, S., & Rhoads, J. E. 2008, ApJ, 673, 686 Hirano, S., Hosokawa, T., Yoshida, N., et al. 2014, ApJ, 781, 60 Hogg, D. W. 1999, arXiv:astro-ph/9905116 Holwerda, B. W., Bouwens, R., Oesch, P., et al. 2015, ApJ, 808, 6 Holwerda, B. W., Bridge, J. S., Steele, R. L., et al. 2020, AJ, 160, 154 Huang, K.-H., Ferguson, H. C., Ravindranath, S., & Su, J. 2013, ApJ, 765, 68 Hunter, J. D. 2007, CSE, 9, 90 Inayoshi, K., Harikane, Y., Inoue, A. K., Li, W., & Ho, L. C. 2022, ApJL, 938, L10

Bouwens, R. J., Illingworth, G. D., van Dokkum, P. G., et al. 2022, ApJ,

```
Isobe, Y., Ouchi, M., Kojima, T., et al. 2021, ApJ, 918, 54
Johnson, B. D., Leja, J., Conroy, C., & Speagle, J. S. 2021, ApJS, 254, 22
Joye, W. A., & Mandel, E. 2003, in ASP Conf. Ser. 295, Astronomical Data
   Analysis Software and Systems XII, ed. H. E. Payne, R. I. Jedrzejewski, &
   R. N. Hook (San Francisco, CA: ASP), 489
Kauffmann, G., Heckman, T. M., White, S. D. M., et al. 2003, MNRAS,
   341, 33
Kawamata, R., Ishigaki, M., Shimasaku, K., et al. 2018, ApJ, 855, 4
Kawamata, R., Ishigaki, M., Shimasaku, K., Oguri, M., & Ouchi, M. 2015,
   ApJ, 804, 103
Kennicutt, R. C. J. 1998, ApJ, 498, 541
Kikuchihara, S., Ouchi, M., Ono, Y., et al. 2020, ApJ, 893, 60
Kim, J.-G., Kim, W.-T., & Ostriker, E. C. 2018, ApJ, 859, 68
Kormendy, J., & Ho, L. C. 2013, ARA&A, 51, 511
Kruijssen, J. M. D. 2014, CQGra, 31, 244006
Labbe, I., van Dokkum, P., Nelson, E., et al. 2023, Natur, 616, 266
Lackner, C. N., & Gunn, J. E. 2012, MNRAS, 421, 2277
Latif, M. A., & Ferrara, A. 2016, PASA, 33, e051
Leethochawalit, N., Trenti, M., Santini, P., et al. 2023, ApJL, 942, L26
Lovell, C. C., Harrison, I., Harikane, Y., Tacchella, S., & Wilkins, S. M. 2023,
   MNRAS, 518, 2511
Madau, P., & Dickinson, M. 2014, ARA&A, 52, 415
McConnachie, A. W. 2012, AJ, 144, 4
Mosleh, M., Williams, R. J., Franx, M., et al. 2012, ApJL, 756, L12
Naidu, R. P., Oesch, P. A., Setton, D. J., et al. 2022b, arXiv:2208.02794
Naidu, R. P., Oesch, P. A., van Dokkum, P., et al. 2022a, ApJL, 940, L14
Nanayakkara, T., Glazebrook, K., Jacobs, C., et al. 2023, ApJL, 947, L26
Newman, A. B., Ellis, R. S., Bundy, K., & Treu, T. 2012, ApJ, 746, 162
Norris, M. A., Kannappan, S. J., Forbes, D. A., et al. 2014, MNRAS, 443, 1151
Oesch, P. A., Bouwens, R. J., Carollo, C. M., et al. 2010, ApJL, 709, L21
Oke, J. B., & Gunn, J. E. 1983, ApJ, 266, 713
Ono, Y., Ouchi, M., Curtis-Lake, E., et al. 2013, ApJ, 777, 155
Onoue, M., Kashikawa, N., Matsuoka, Y., et al. 2019, ApJ, 880, 77
Ouchi, M., Ono, Y., & Shibuya, T. 2020, ARA&A, 58, 617
Peng, C. Y., Ho, L. C., Impey, C. D., & Rix, H.-W. 2002, AJ, 124, 266
Peng, C. Y., Ho, L. C., Impey, C. D., & Rix, H.-W. 2010, AJ, 139, 2097
Perrin, M. D., Sivaramakrishnan, A., Lajoie, C.-P., et al. 2014, Proc. SPIE,
  9143, 91433X
Perrin, M. D., Soummer, R., Elliott, E. M., Lallo, M. D., &
   Sivaramakrishnan, A. 2012, Proc. SPIE, 8442, 84423D
Planck Collaboration, Aghanim, N., Akrami, Y., et al. 2020, A&A, 641, A6
Pontoppidan, K. M., Barrientes, J., Blome, C., et al. 2022, ApJL, 936, L14
Rieke, M. J., Kelly, D., & Horner, S. 2005, Proc. SPIE, 5904, 1
Rigby, J., Perrin, M., McElwain, M., et al. 2023, PASP, 135, 048001
```

```
Robertson, B. E. 2022, ARA&A, 60, 121
Rodriguez-Gomez, V., Genel, S., Vogelsberger, M., et al. 2015, MNRAS,
  449, 49
Rybicki, G. B., & Lightman, A. P. 1979, Radiative Processes in Astrophysics
  (New York: Wiley)
Salim, S., Rich, R. M., Charlot, S., et al. 2007, ApJS, 173, 267
Salmon, B., Coe, D., Bradley, L., et al. 2018, ApJL, 864, L22
Salpeter, E. E. 1955, ApJ, 121, 161
Sameie, O., Boylan-Kolchin, M., Hopkins, P. F., et al. 2023, MNRAS,
  522, 1800
Sersic, J. L. 1968, Atlas de Galaxias Australes (Cordoba: Observatorio
  Astronomico)
Shakura, N. I., & Sunyaev, R. A. 1976, MNRAS, 175, 613
Shen, Y., Wu, J., Jiang, L., et al. 2019, ApJ, 873, 35
Shibuya, T., Ouchi, M., & Harikane, Y. 2015, ApJS, 219, 15
Somerville, R. S., Olsen, C., Yung, L. Y. A., et al. 2021, MNRAS, 502, 4858
Steidel, C. C., Adelberger, K. L., Giavalisco, M., Dickinson, M., & Pettini, M.
  1999, ApJ, 519, 1
Tacchella, S., Dekel, A., Carollo, C. M., et al. 2016, MNRAS, 457, 2790
Tacchella, S., Eisenstein, D. J., Hainline, K., et al. 2023, arXiv:2302.07234
Tacconi, L. J., Neri, R., Genzel, R., et al. 2013, ApJ, 768, 74
Tody, D. 1986, Proc. SPIE, 627, 733
Tody, D. 1993, in ASP Conf. Ser. 52, Astronomical Data Analysis Software
  and Systems II, ed. R. J. Hanisch, R. J. V. Brissenden, & J. Barnes (San
  Francisco, CA: ASP), 173
Topping, M. W., Stark, D. P., Endsley, R., et al. 2022, ApJ, 941, 153
Treu, T., Roberts-Borsani, G., Bradac, M., et al. 2022, ApJ, 935, 110
van Dokkum, P. G., Abraham, R., Merritt, A., et al. 2015, ApJL, 798, L45
Virtanen, P., Gommers, R., Oliphant, T. E., et al. 2020, NatMe, 17, 261
Wang, F., Yang, J., Fan, X., et al. 2021, ApJL, 907, L1
Whitler, L., Endsley, R., Stark, D. P., et al. 2023, MNRAS, 519, 157
Wright, E. L. 2006, PASP, 118, 1711
Wu, X.-B., Wang, F., Fan, X., et al. 2015, Natur, 518, 512
Xu, H., Wise, J. H., Norman, M. L., Ahn, K., & O'Shea, B. W. 2016, ApJ,
  833, 84
Yajima, H., Abe, M., Fukushima, H., et al. 2022a, arXiv:2211.12970
Yajima, H., Abe, M., Khochfar, S., et al. 2022b, MNRAS, 509, 4037
Yan, H., Ma, Z., Ling, C., Cheng, C., & Huang, J.-S. 2023, ApJL, 942, L9
Yang, J., Wang, F., Fan, X., et al. 2020, ApJL, 897, L14
Yang, J., Wang, F., Fan, X., et al. 2021, ApJ, 923, 262
Yang, L., Morishita, T., Leethochawalit, N., et al. 2022, ApJL, 938, L17
Yung, L. Y. A., Somerville, R. S., Ferguson, H. C., et al. 2022, MNRAS,
  515, 5416
Zolotov, A., Dekel, A., Mandelker, N., et al. 2015, MNRAS, 450, 2327
```